Project Report
EO-1-4

Earth Observing-1 Advanced Land Imager: Detector Line-of-Sight Calibration

D.R. Hearn

NMP-00961
FILE COPY

29 December 2000

Lincoln Laboratory
MASSACHUSETTS INSTITUTE OF TECHNOLOGY
LEXINGTON, MASSACHUSETTS

Prepared for the National Aeronautics and Space Administration, Goddard Space Flight Center, under Air Force Contract F19628-00-C-0002.

This document is available to the public through the National Technical Information Service, Springfield, Virginia 22161.

The work reported in this document was performed at Lincoln Laboratory, a center for research operated by Massachusetts Institute of Technology. The work was sponsored by the National Aeronautics and Space Administration, Goddard Space Flight Center, under Air Force Contract F19628-00-C-0002.

TECHNICAL REPORT STANDARD TITLE PAGE

1. Report No. EO-1-4	2. Government Accession No.	3. Recipient's Catalog No.
4. Title and Subtitle Earth Observing-1 Advanced Land Imager: Detector Line-of-Sight Calibration		5. Report Date 29 December 2000 6. Performing Organization Code
7. Author(s) D.R. Hearn		8. Performing Organization Report No. EO-1-4
9. Performing Organization Name and Address MIT Lincoln Laboratory 244 Wood Street Lexington, MA 02420-9108		10. Work Unit No. (TRAIS) 11. Contract or Grant No. F19628-00-C-0002
12. Sponsoring Agency Name and Address National Aeronautics and Space Administration/GSFC Mr. Ralph Welsh Building 16, Room 21 MS 740.3 Greenbelt, MD 20771		13. Type of Report and Period Covered Project Report 14. Sponsoring Agency Code

15. Supplementary Notes

This report is based on studies performed at Lincoln Laboratory, a center for research operated by Massachusetts Institute of Technology, under Air Force Contract F19628-00-C-0002.

16. Abstract

The Advanced Land Imager (ALI) of the Earth Observing-1 (EO-1) satellite has been extensively calibrated at Lincoln Laboratory, where it was designed and integrated. The calibrations performed were radiometric, spectral, and spatial in nature. This report describes the spatial calibration of the detector lines-of-sight. Relevant details of the ALI instrument design are presented first. Measurements made on the focal plane array geometry and the optical distortions of the telescope are described next. End-to-end measurements of the complete instrument were performed by recording and analyzing static images of a Ronchi ruling. The resulting detector line-of-sight (LOS) map is described, and a linear approximation to the optical distortion is discussed. Finally, the process of making and analyzing theodolite measurements of the orientation of the telescope optical axes relative to the ALI external reference cube is described in some detail.

17. Key Words	18. Distribution Statement This doucment is available to the public through the National Technical Information Service, Springfield, VA 22161.

19. Security Classif. (of this report)	20. Security Classif. (of this page)	21. No. of Pages	22. Price
Unclassified	Unclassified	72	

FORM DOT F 1700.7 (8-72) Reproduction of completed page authorized

ABSTRACT

The Advanced Land Imager (ALI) of the Earth Observing-1 (EO-1) satellite has been extensively calibrated at Lincoln Laboratory, where it was designed and integrated. The calibrations performed were radiometric, spectral, and spatial in nature. This report describes the spatial calibration of the detector lines-of-sight. Relevant details of the ALI instrument design are presented first. Measurements made on the focal plane array geometry and the optical distortions of the telescope are described next. End-to-end measurements of the complete instrument were performed by recording and analyzing static images of a Ronchi ruling. The resulting detector line-of-sight (LOS) map is described, and a linear approximation to the optical distortion is discussed. Finally, the process of making and analyzing theodolite measurements of the orientation of the telescope optical axes relative to the ALI external reference cube is described in some detail.

ACKNOWLEDGMENTS

The author is indebted to the many individuals who contributed to the integration and calibration of the ALI. At Lincoln Laboratory, Bert Willard designed the imaging collimator that made the line-of-sight calibrations possible. Jeff Mendenhall was instrumental in setting up and operating the computer equipment and LabVIEW software to record the calibration data. Ron Sayer developed the data recording software. Scott Stuart made major contributions in structuring the least-squares fitting software, and implementing the use of MPFIT to make it flexible and powerful.

From Raytheon Santa Barbara Remote Sensing, Cliff Nichols and Paul Bryant supplied the focal plane measurement data. Bryan Norman and Vicky Loriaux of SSG performed the measurements on the telescope optics.

TABLE OF CONTENTS

	Abstract	iii
	Acknowledgments	v
	List of Illustrations	ix
	List of Tables	xi
1	INTRODUCTION	1
2	SYSTEM DESCRIPTION	3
	2.1 Optical System	3
	2.2 Detector system	4
	2.3 Detector Line-of Sight Model	8
	2.4 Reference Cube	9
3	SUBSYSTEM MEASUREMENTS	11
	3.1 Focal Plane Subsystem	11
	3.2 Optical Subsystem	12
4	END-TO-END LOS CALIBRATION	17
	4.1 Measurement setup	17
	4.2 Analysis of Measurements	18
5	DETECTOR LINE-OF-SIGHT MAP	29
	5.1 Line-of-Sight Map File Contents	29
	5.2 Simple Image Reconstruction	29
	5.3 Test Images	30
6	SPECTRAL PURITY	33
	6.1 Linear Approximation of the Optical Distortion	33
	6.2 Operational Implications for the ALI	34
	6.3 Implications for Future Land Imagers	38

TABLE OF CONTENTS (Continued)

7 REFERENCE CUBE ALIGNMENT 39

7.1 Basic Setup 40
7.2 Procedure 40
7.3 Angular Measurements 42
7.4 Rotation to Cube-Based Coordinates 44
7.5 Telescope Optical Axes in the Cube Reference Frame 47

APPENDIX A. ALI LINE-OF-SIGHT PARAMETERS 51

Glossary 57
References 59

LIST OF ILLUSTRATIONS

Figure No.		Page
1	Ray diagram of the ALI telescope in the spacecraft X-Z plane, omitting the final fold flat mirror.	3
2	Ray diagram of the ALI telescope in the spacecraft Y-Z plane, omitting the final fold flat mirror.	4
3	ALI Focal Plane Array assembly.	5
4	MS/Pan detector module assembly.	5
5	Arrangement of the SCA's on the focal plane.	6
6	Layout of the detectors on the sensor chip assemblies.	7
7	Close-up cross-section of the MS/Pan filter-detector assembly in the X-Z plane.	8
8	Focal plane surrogate fixture used for SSG measurements.	13
9	ALI telescope optical distortion, from SSG measurement data.	15
10	Residual ALI optical distortion, after subtracting a cubic polynomial fit from the measurement data.	15
11	Top view of the imaging collimator used for spatial calibrations of the ALI.	17
12	Flow chart of losfunct_2.pro, the function procedure to compute modeled detector signals and subtract them from the measured detector signals.	20
13	Measured detector signals and modeled signals (in red) for the Pan Band, 59.47° Ronchi orientation.	22
14	Measured detector signals and modeled signals (in red) for Band 7, 0.33° Ronchi orientation.	23
15	Comparison plots of optical distortion over the entire ALI field of view.	25

LIST OF ILLUSTRATIONS (Continued)

Figure No.		Page
16	Displacements of the sensor chips from their designed locations.	26
17	Vector plot of the MS/Pan end of the focal plane.	27
18	Reconstructed ALI image recorded from a photographic transparency scan.	31
19	Pan band image of the Ronchi ruling at 60°.	32
20	Residual optical distortion around the MS/Pan detector array, after application of a linear coordinate transformation.	34
21	Sampling mismatches from Band 1′ to Band 7, optimized for entire MS array.	35
22	Sampling mismatches from Band 1′ to Band 7, optimized for SCA 4.	36
23	Spectral purity defined as overlap area (sketch).	37
24	Spectral purity from Band 1′ to Band 7, optimized for entire MS array.	37
25	Spectral purity from Band 1′ to Band 7, optimized for SCA 4.	38
26	Plan view of clean room setup to measure alignment of the ALI reference cube.	39
27	View of the ALI focal plane, as seen through the telescope.	41
28	Sight pictures through the theodolite when the crosshairs are correctly aligned with either end of the Pan detector sub-array.	41

LIST OF TABLES

Table N		Page
	Measured Loca cf .A 'iducial Marks, ALI 'ocal Plane Coo	
	AL. Coordinates of SCA iducial A, and Rotation Angl	
	escope Distorti Measurement Data	
	Angular Readings of the Pan Detector Array Degrees	
	Angular Readings of the R ference Cube Degrees	44
	ighting Vect the Laboratory rame	
	Direction Vectors the Cube Fr	
	Direction th Telescope ram	
A	R chi Ruling Collimator Parameters	
A-2	hip Assembly Positi Design Parameters	
A-3	Sensor Chip Assembly osition Offset Parameters	
A-4	SWIR Detector Chip osition Offset arameters	54
A	ALI Telescope Parameters	
A-6	Coeffi ents of the Distorti olynomials,	
A	Coeffi of the Distortion lynomials B	

1 INTRODUCTION

The Advanced Land Imager (ALI) of the EO-1 satellite has been described by Digenis, et al.[1]. General descriptions of the calibration of this instrument have been given in several papers [2], [3], [4]. An overview of the spatial calibrations has also been presented [5]. The preflight calibration measurements were completed prior to instrument delivery. The analysis of those measurements has now also been completed. This report describes the detector line-of-sight calibrations.

In order to reconstruct the ALI image data in reference to the geographic coordinates of the land scene, many pieces of information are required. The position of the satellite and its attitude (pointing direction) at the instant of observation obviously must be known. Equally important, the lines-of-sight (LOS) of the many detectors, relative to the satellite body axes must be known. That information is contained in the LOS map.

The next section describes the key features of the ALI telescope and focal plane systems. The sections which follow cover the measurement setups and equipment, the analysis of the raw measurements, and the detector LOS map which has been derived. An additional section describes spectral purity, a linear approximation to the optical distortion, and its significance for future land imaging instruments of this type. Finally, the determination of the angular relationship of the relative detector lines-of-sight to the external ALI reference cube is described.

2 SYSTEM DESCRIPTION

2.1 OPTICAL SYSTEM

The telescope of the Advanced Land Imager is a three-mirror anastigmat, designed and built by SSG, Inc. Its field of view is 15° in the cross-track direction, and 1.24° in the in-track direction. Its focal length was nominally specified to be 940 mm. The mirrors are displaced and tilted from the optical axis. As a result, the optical distortions are not axisymmetric. Ray diagrams of the telescope are shown in Figure 1and Figure 2.

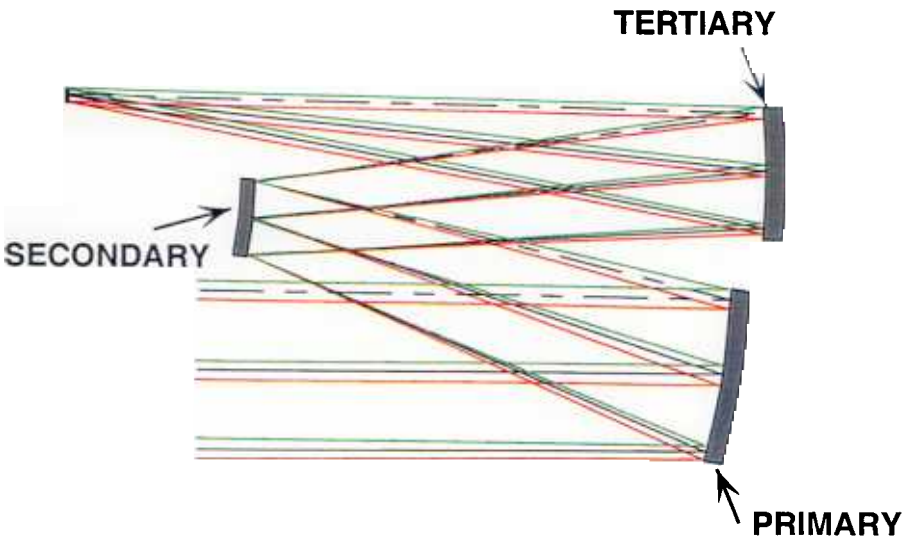

Figure 1. Ray diagram of the ALI telescope in the spacecraft X-Z plane, omitting the final fold flat mirror.

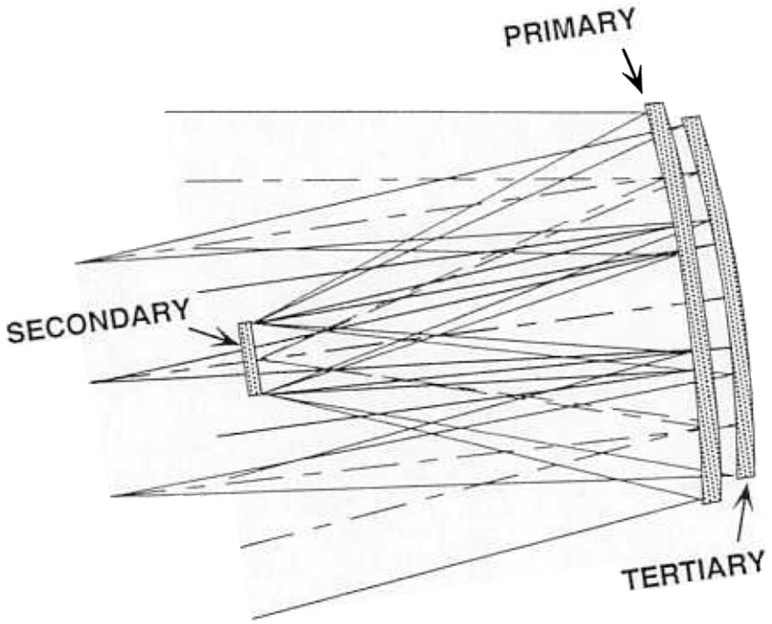

Figure Ray diagram of the ALI telescope in the spacecraft Y-Z plane, omitting the final fold flat mirror

2.2 DETECTOR SYSTEM

The detector subsystem of the ALI, also called the focal plane array (FPA), was designed and built to the MIT Lincoln Laboratory specification by Raytheon Santa Barbara Remote Sensing (SBRS). Its main components are the focal plane electronics unit, and the detector subassembly shown in Figure 3, mounted on a passively-cooled beryllium rail. The rail carries five modular subassemblies, on which are mounted the silicon sensor chip assemblies (SCA's) themselves. As the EO-1 is only to demonstrate technological feasibility of the basic design, only one of the modules, at the edge of the field-of-view, carries active SCA's. That module is depicted in figure 4.

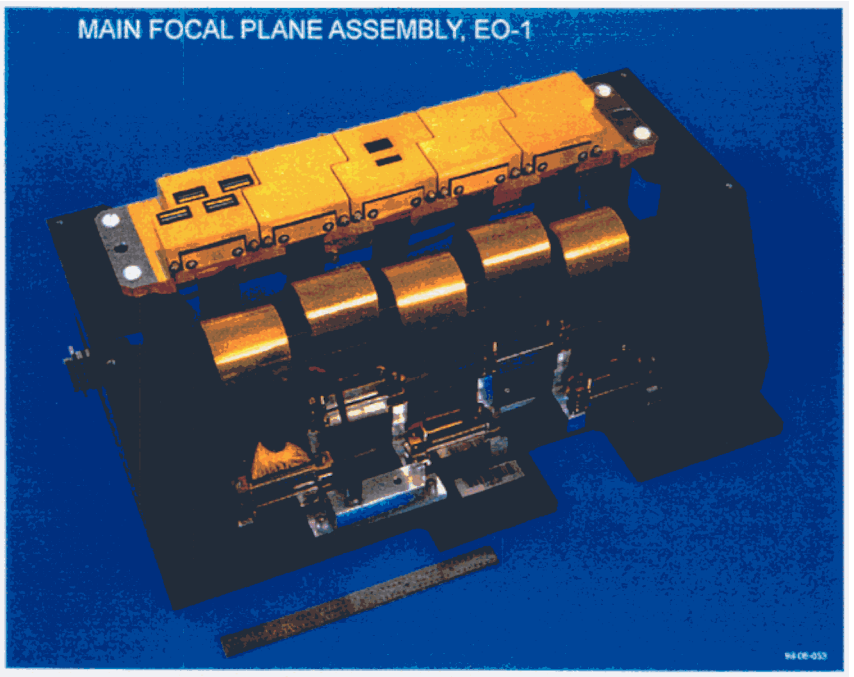

Figure 3. ALI Focal Plane Array assembly.

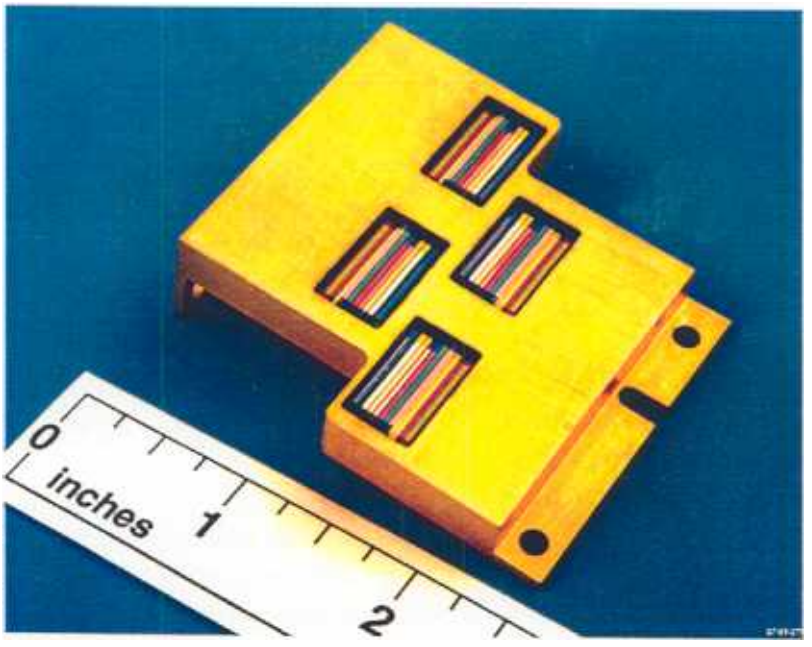

Figure 4. MS/Pan detector module assembly.

The active module has four sensor chip assemblies. They are staggered, in order to provide for overlap of coverage between the neighboring SCA's. The general locations of the SCA's are shown in Figure 5, and detailed dimensions of the detectors are given in Figure 6. Each SCA includes one panchromatic (Pan) band, with a basic detector pitch of 13.2 μm, and nine multispectral (MS) bands, with a basic detector pitch of 39.6 μm by 40 μm. The Pan band has 960 detectors across the SCA, and each MS band has 320 detectors across. Together, the four SCA's comprise the MS/Pan array. In operation, the ALI is pointed in the nadir direction, and the motion of the satellite scans the detector array over the scene in a push-broom mode.

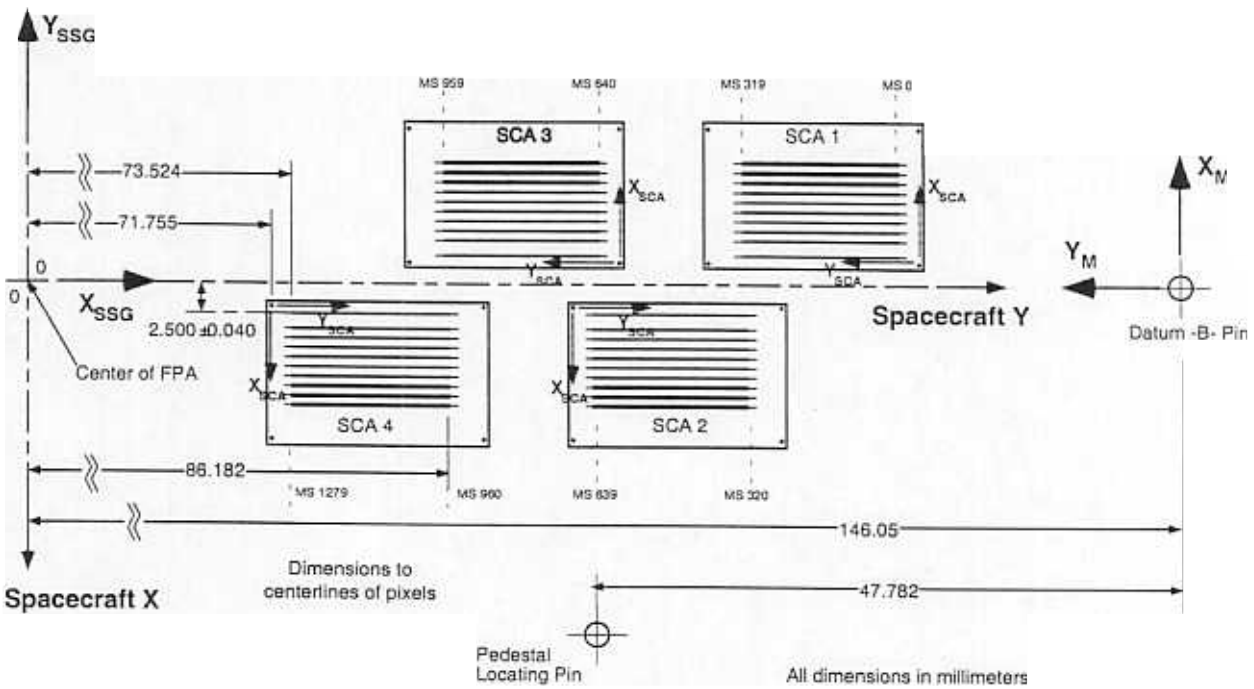

Figure 5. Arrangement of the SCA's on the focal plane.

Bands in the visible and near-infrared (VNIR) part of the spectrum utilize Silicon-PIN photodiodes formed within the silicon read-out integrated circuit (ROIC). The short-wave infrared (SWIR) bands have HgCdTe detectors in a chip that is indium bump-bonded to the ROIC. Each detector is coupled to a capacitive transimpedance amplifier in the ROIC.

Spectral response of the various bands is governed by an assembly of band-pass filters mounted to the bezel assembly covering the detector module. The substrates of the filters are of various thicknesses in order to maintain a constant longitudinal focus shift. A large-scale cross-section of the filters and SCA at the transition from VNIR (Band 4′) to SWIR (Band 5′) detectors is shown in Figure 7.

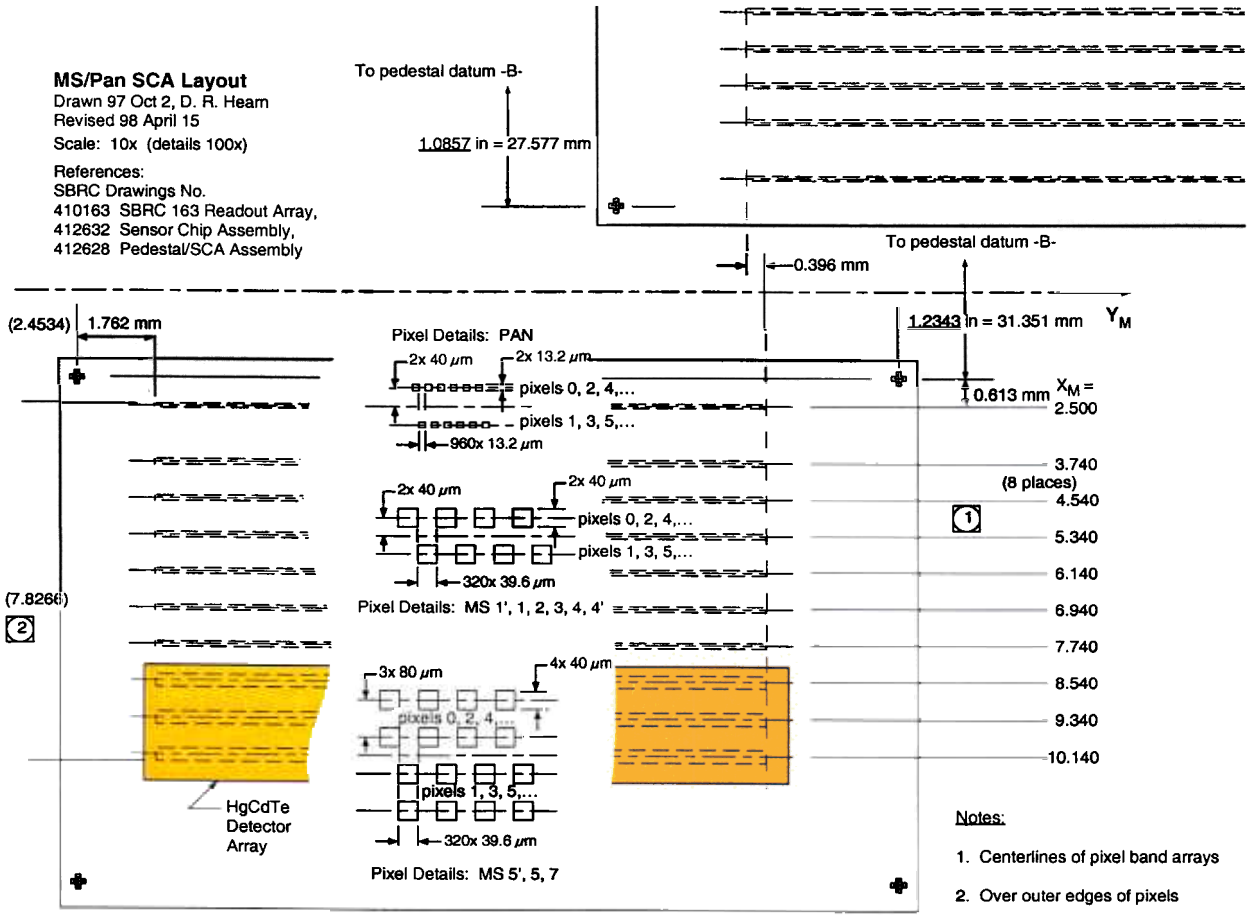

Figure 6. Layout of the detectors on the sensor chip assemblies.

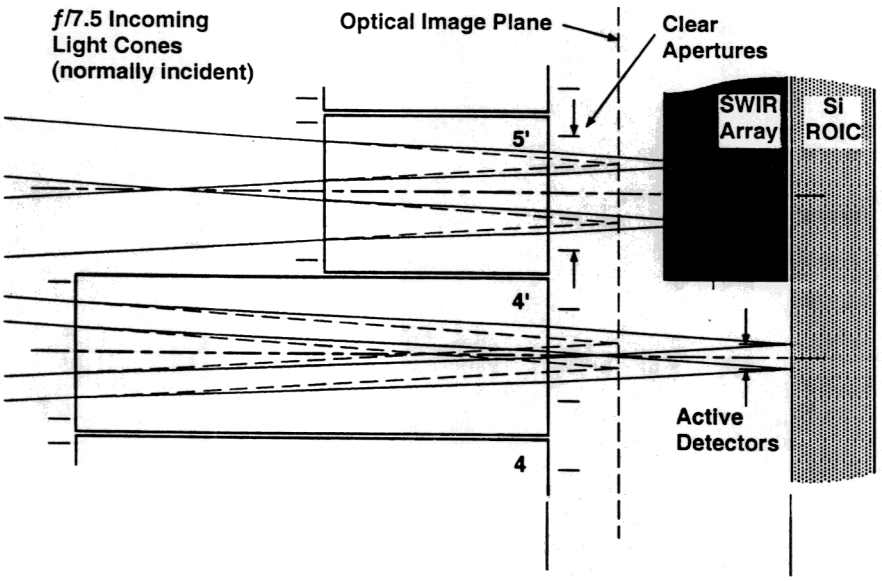

Figure 7. Close-up cross-section of the MS/Pan filter-detector assembly in the X-Z plane.

2.3 DETECTOR LINE-OF SIGHT MODEL

The goal of the present detector LOS calibration is to develop a tabulation of the sight direction of each detector on the ALI focal plane, relative to a set of reference axes. The resulting look-up table would then be used in conjunction with satellite position and attitude data in the reconstruction of geo-referenced images from the radiometrically-calibrated detector signals. The ALI focal plane carries 3,840 Pan detectors, and 11,520 multispectral detectors. We considered it impractical to measure directly the LOS of each individual detector. Instead, a parameterized model was developed to describe the apparent position of each detector on the focal plane, as seen through the telescope. Our detector LOS map is a tabulation of those apparent positions. To obtain the angular LOS of any detector, we treat the telescope as an ideal imaging system, with a given focal length.

The focal length of the telescope is one obvious parameter. The physical position of a detector on the focal plane is described by the positions of fiducial marks on the SCA, and the layout design of the SCA. Here, we assume that the geometric precision of the photolithographic process used to make the ROIC/detector chip is on the order of 0.1 μm, far greater than our ability to discern errors. Each VNIR detector thus far has four uncertain parameters to determine its position: focal length of the telescope,

X–offset, Y–offset, and rotation offset of the SCA. In the case of the SWIR bands, three additional parameters describe the offset of the SWIR detector array chip relative to the ROIC.

Even if fabricated perfectly, the ALI telescope design produces some optical distortion. Owing to the asymmetry of the design, the distortion is not axisymmetric. Thus we are unable to apply a simple radial distortion model. Instead, we resort to a general third-order polynomial in X (the in-track axis) and Y (the cross-track axis). There are actually two polynomials, one for the X component of the distortion, and one for the Y component. This leads potentially to 32 polynomial coefficients to be determined. At least, some of the coefficients can be eliminated, such as the zero-power term, representing a fixed offset. Still, a large number are left. It may be asked whether cubic polynomials are sufficient? As a practical matter, good fits to the measurements appear to be achieved with them.

The fixed or fitted values of all parameters in the line-of-sight model are listed in Appendix A.

2.4 REFERENCE CUBE

Finally, The ALI includes an optical reference cube fixed to its base pallet. Section 7 of this report describes the measurements that were made by theodolite to determine the orientation of the optical axes of the ALI telescope relative to this ALI reference cube. After final integration with the spacecraft, additional theodolite measurements were made to relate the ALI reference cube to the other sensors on board the spacecraft.

3 SUBSYSTEM MEASUREMENTS

Four distinct sets of measurements were made in order to estimate the values of the line-of-sight parameters. This section describes the measurements made on the major subsystems of the instrument. SBRS measured the locations of the SCA's on the assembled MS/Pan module, and SSG used a precision theodolite and a substitute focal plane fixture to measure the telescope for focal length and distortions.

Section 4 describes the end-to-end calibration measurements of the complete instrument to establish the detector lines-of-sight relative to the telescope axes. Finally, Section 7 discusses the theodolite measurements at Lincoln Laboratory to establish the angles from the reference cube to the telescope axes.

3.1 FOCAL PLANE SUBSYSTEM

TABLE 1

Measured Locations of SCA Fiducial Marks, in ALI Focal Plane Coordinates

	X (mm)	Y (mm)
SCA1		
Fiducial A	-1.8898	124.7800
Fiducial B	-1.8898	107.5781
SCA2		
Fiducial A	1.8885	96.3102
Fiducial B	1.8875	113.5083
SCA3		
Fiducial A	-1.8915	100.2231
Fiducial B	-1.8920	83.0229
SCA4		
Fiducial A	1.8875	71.7530
Fiducial B	1.8875	88.9541

The subsystem measurements by Santa Barbara Remote Sensing (SBRS) on the assembled focal plane used a coordinate-measuring machine to establish the locations of fiducial marks in the metallization of each SCA, to an accuracy of ~ ± 1 μm. The location measurements, translated to the ALI focal plane coordinates, are listed in TABLE 1. TABLE 2 shows the comparison between the designed locations and the measured locations of the "A" fiducial marks and rotation angle. The location of the pixels within each SCA, determined by photolithography, is believed to have an accuracy of ~ ± 0.1 μm.

TABLE 2

ALI Coordinates of SCA Fiducial "A," and Rotation Angles

	SCA1	SCA2	SCA3	SCA4
Nominal Values				
X (mm)	-1.887	1.887	-1.887	1.887
Y (mm)	124.780	96.309	100.226	71.755
Omega (°)	180.00	0.00	180.00	0.00
Fitted Values				
X (mm)	-1.8898	1.8885	-1.8915	1.8875
Y (mm)	124.7791	96.3092	100.2230	71.7535
Omega (°)	180.0000	-0.0034	-179.9983	0.0000
Departure from Nominal Values				
X (μm)	-2.76	1.49	-4.54	0.47
Y (μm)	-0.91	0.24	-2.99	-1.46
Omega (mrad)	0.000	-0.059	0.030	0.000

3.2 OPTICAL SUBSYSTEM

To characterize the telescope distortion, a fixture bearing scribed lines was mounted at the focal plane location. (See Figure 8.) These lines were measured at Lincoln Laboratory on a coordinate-measuring machine. A precision theodolite was used to measure the angles of the scribe-line intersections when seen through the telescope, to ± 1 arc sec. The measured numbers are listed in TABLE 3. These

angular readings were then fitted to cubic polynomial functions to describe the cross-track and in-track optical distortion. A vector map of the measured distortions is shown in Figure 9. The axes are labeled in millimeters, and encompass the entire 15°x1.2° field of view of the telescope. The longest vector represents 0.928 mm of distortion at the focal plane. The residuals from the fits are shown in Figure 10. The fitted focal lengths are 942.41 mm and 945.15 mm in the cross-track and in-track directions, respectively. The scale of the vectors is greatly enlarged in comparison with Figure 9.

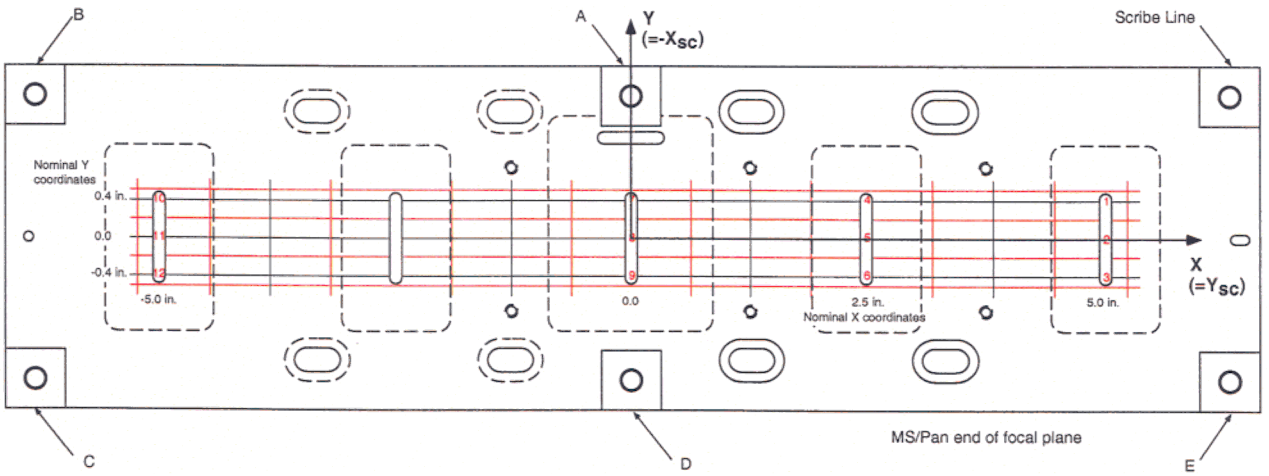

Figure 8. Focal plane surrogate fixture used for SSG measurements.

TABLE 3

Telescope Distortion Measurement Data

Point	Angles (deg.)		Linear Position (in.)		Point	Angles (deg.)		Linear Position (in.)	
	alpha	beta	X ($-Y_m'$)	Y (X_m)		alpha	beta	X ($-Y_m'$)	Y (X_m)
1	66.293	2.080	5.1207	0.4945	21	75.135	1.926	-0.6233	0.4953
2	66.282	1.633	5.1209	0.2023	22	75.129	1.474	-0.6234	0.2013
3	66.267	1.019	5.1206	-0.1997	23	75.120	0.852	-0.6237	-0.2026
4	66.257	0.570	5.1200	-0.4926	24	75.111	0.399	-0.6227	-0.4969
5	67.574	2.055	4.2854	0.4939	25	77.010	1.898	-1.8372	0.4949
6	67.565	1.606	4.2852	0.2017	26	77.003	1.445	-1.8375	0.2013
7	67.550	0.991	4.2853	-0.2004	27	76.995	0.825	-1.8378	-0.2032
8	67.538	0.543	4.2859	-0.4927	28	76.989	0.371	-1.8385	-0.4978
9	69.438	2.018	3.0630	0.4931	29	78.898	1.872	-3.0631	0.4956
10	69.444	1.568	3.0620	0.2009	30	78.894	1.421	-3.0632	0.2013
11	69.431	0.952	3.0621	-0.2012	31	78.887	0.799	-3.0635	-0.2032
12	69.423	0.502	3.0610	-0.4935	32	78.878	0.344	-3.0624	-0.4980
13	71.336	1.986	1.8397	0.4936	33	80.775	1.852	-4.2834	0.4970
14	71.328	1.536	1.8388	0.2009	34	80.774	1.400	-4.2841	0.2023
15	71.318	0.916	1.8387	-0.2015	35	80.770	0.779	-4.2843	-0.2035
16	71.308	0.466	1.8389	-0.4945	36	80.766	0.325	-4.2848	-0.4993
17	73.226	1.957	0.6143	0.4959	37	82.064	1.841	-5.1208	0.4987
18	73.219	1.504	0.6137	0.2020	38	82.061	1.389	-5.1221	0.2033
19	73.210	0.882	0.6128	-0.2019	39	82.059	0.765	-5.1222	-0.2033
20	73.199	0.430	0.6140	-0.4956	40	82.055	0.311	-5.1224	-0.5006

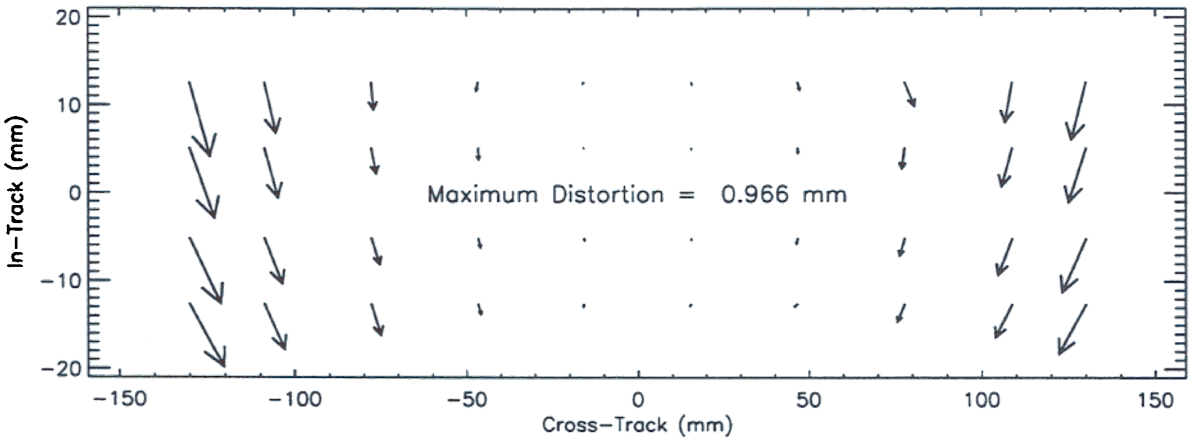

Figure 9. ALI telescope optical distortion, from SSG measurement data.

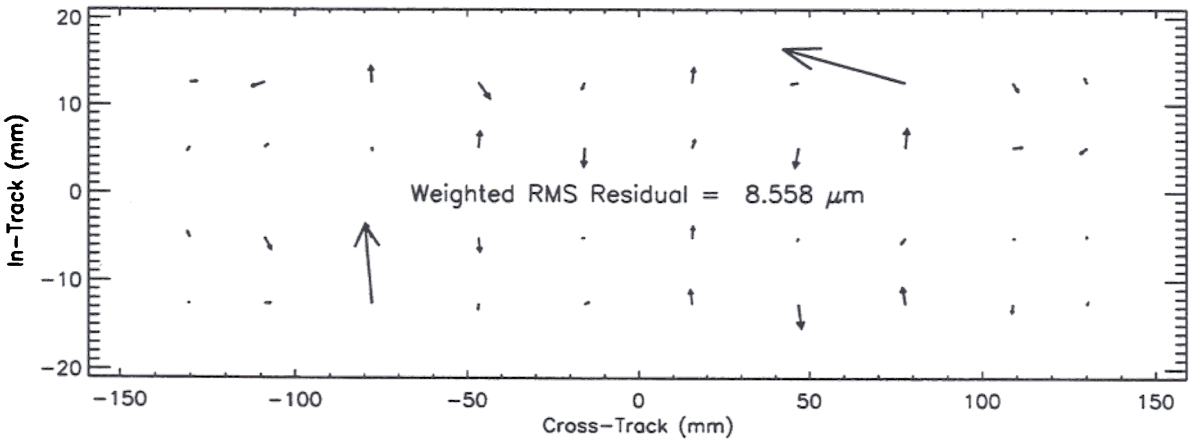

Figure 10. Residual ALI optical distortion, after subtracting a cubic polynomial fit from the measurement data.

4 END-TO-END LOS CALIBRATION

4.1 MEASUREMENT SETUP

Measurements on the integrated ALI instrument were carried out in a Class 1,000 clean room at Lincoln Laboratory. The relative detector LOS measurements were done while the ALI was in a thermal vacuum chamber, operating at nominal flight conditions. An imaging collimator was placed outside the window of the vacuum chamber, with its un-obscured exit pupil in coincidence with the virtual entrance pupil of the ALI instrument. It has diffraction-limited performance over a 3.2° field of view. This Schmidt-sphere imaging collimator is fully described by Willard [6]. The methods used to establish the collimation of the output beam are also described in that reference. A layout of the collimator bench is shown in Figure 11. The light source is a 250 W quartz tungsten halogen lamp, with a 6-inch integrating sphere behind the condensing lens. The exit port of the integrating sphere forms the pupil of the collimator, in order to illuminate the ALI entrance pupil uniformly.

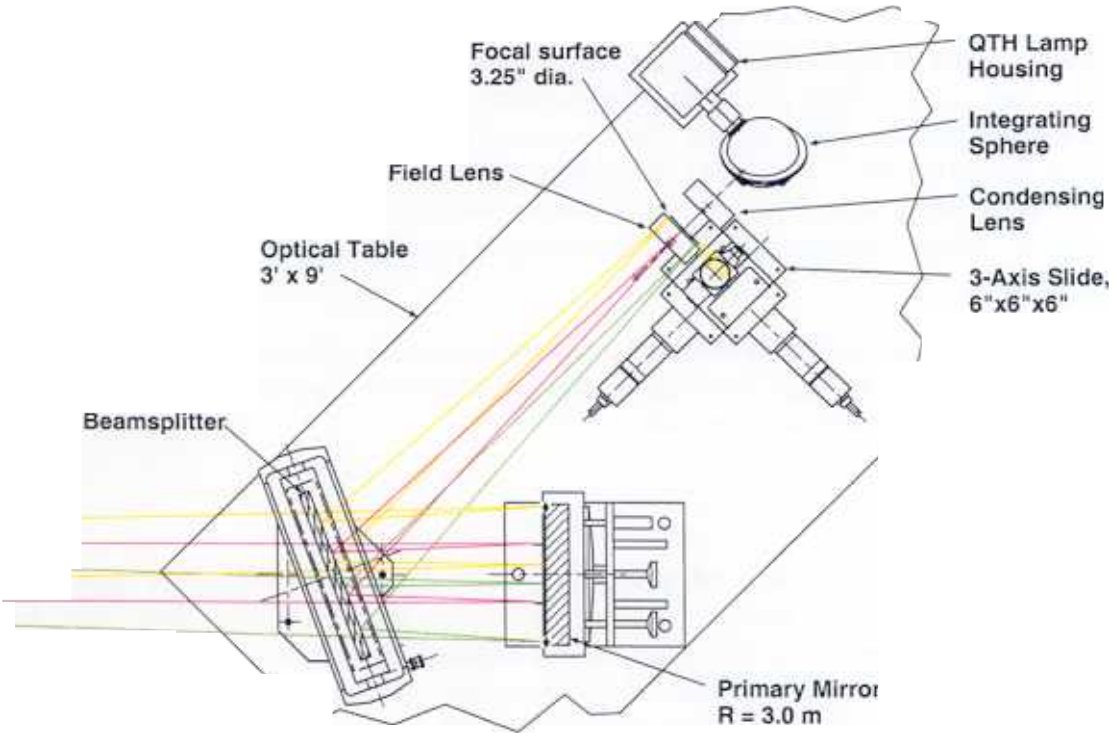

Figure 11. Top view of the imaging collimator used for spatial calibrations of the ALI.

A precision target was placed at the collimator focal plane. We sought a target pattern which would provide detector signals sensitive to the various line-of-sight parameters. Ordinarily, a standard grid target would be used, giving apparent displacements of the grid points as seen by the instrument. The ALI detectors are arranged on the focal plane in staggered rows, not in a simple two-dimensional grid. It is only capable of forming two-dimensional images by scanning. It was undesirable to scan the target with the vertical slide, as was done to test end-to-end image formation, since that would introduce the uncertainties of the scan speed and direction. It was thus not feasible to measure the relative lines of sight with a standard grid target placed at the collimator focal plane. The approach chosen was to record static images of a Ronchi ruling placed at the collimator focal plane. The orientation of the ruling was changed from one image to the next. First, the lines were vertical, in the in-track direction to the ALI. Two more images were recorded with the lines at approximately 60° and 120° from vertical. The three static images of the Ronchi ruling which were later analyzed consisted of averages of 1,000 frames of MS/Pan detector signals. An image was also recorded with the Ronchi ruling removed from the collimator, to establish the "white" level signals. Similarly, dark levels were recorded, with the aperture cover of the instrument closed.

4.2 ANALYSIS OF MEASUREMENTS

Relative lines of sight of the detectors were estimated from the Ronchi ruling images by using a linearized, least-squares fitting process to adjust the LOS parameters until numerically modeled detector signals matched the measured signals. The frequency of the Ronchi ruling target mounted in the collimator was 2.000 mm^{-1}. At the ALI focal plane, this became approximately 3.18 mm^{-1}. Thus there were 40.2 cycles of the ruling across each SCA detector row for the vertical ruling, and 20.1 cycles for the 60° and 120° rulings. This was expected to provide great precision in determining the relative detector lines-of-sight.

The data from the ALI were recorded and pre-processed on a Silicon Graphics workstation. The raw files were archived to digital linear tape. Additional analysis was performed with the IDL language, running on a 500 MHz Power Macintosh G4.

4.2.1 Signal Estimation

An advantage of the Ronchi ruling target is the simplicity of modeling the expected detector signals. A disadvantage is the ambiguity in the relative ruling phase (number of lines) from one row of detectors to a different row. The ambiguity was not expected to be a problem, since the relative SCA positions were estimated to ±5 μm from subsystem measurements, and the period of the ruling at the SCA's was at least 300 μm. By the time the Ronchi ruling images were finally analyzed, we had the results of the laboratory modulation transfer function measurements on the ALI [7]. Given a spatial frequency and orientation for the Ronchi ruling, the two-dimensional spatial transfer function for each detector spectral band was interpolated at the discrete set of frequencies contained in the Ronchi square-

wave pattern. In IDL, the product of the detector transfer function with the component amplitudes of the square-wave was inverse-Fourier transformed to construct the detector response as a function of phase within the Ronchi cycle. This was stored as a look-up table. The remainder of the calculations then used vector algebra to find the expected phase of the Ronchi cycle at each detector.

The raw detector signals were radiometrically corrected with a simple two-point calibration. First, background dark-level values were subtracted from the raw signals. This was also done to a "white" image recorded with the Ronchi ruling removed from the collimator. The dark-subtracted Ronchi signals were then normalized by dividing by the corresponding white signals. We found that the signals thus normalized did not show a uniform level of peak values, but slowly varied from about 70% to 90% across the field of view. Similarly, the dark lines did not drop to zero, but instead approximately to 10 to 15% of the peak levels. Only the relative positions of the Ronchi ruling lines were of interest here, and not the signal levels in the "white" and "black" parts of the ruling. Therefore, an additional "re-normalization" was performed on the detector signals, to cause the peaks to be near one, and the valleys near zero. The theoretical response *vs.* Ronchi phase array (which also did not range from zero to one) was modified to match.

4.2.2 Least-Squares Parameter Fitting

In the standard IDL package is a linearized, least-squares fitting procedure called *curvefit.pro*. It requires the user to supply a function of the independent variables to be fitted to a given set of measured data values. Any number or type of parameters may be used to describe the user's function. In this case, the data values are the (re-normalized) measured detector signals for *all three* static Ronchi images, and the independent variables are the identities of the detectors to be fitted. The parameters of the user function include all of those listed in Section 2.3 (Detector Line-of Sight Model). The SCA 4 fiducial position was selected to be fixed, to anchor the coordinate system of the telescope. In addition, there are further parameters to describe the setup conditions of each image: the relative azimuth and elevation of the collimator, the focal length of the collimator, and the frequency, orientation angle, and on-axis phase of the Ronchi ruling.

An enhanced least-squares fitting procedure, also in IDL, called *mpfit.pro* was used here in preference to *curvefit.pro* [8]. Among many other features, *mpfit* permits the user to fix individual parameters so that they do not take part in the fitting process. This was very useful in getting the fits to converge successfully. A flow-chart for the user-supplied function procedure we called *losfunct_2.pro* is shown in Figure 12. Initial parameter estimates were stored in a file to be read by the top-level analysis program. The input parameter file also specifies which detector signals are to be fitted.

Vector algebra was used to trace the ray from the center of each detector through the ALI telescope, and through the collimator to its intersection with the Ronchi ruling target. Both the ALI optical system and the collimator were treated as ideal imaging systems with added distortion. Angular rotations of the vectors to different reference frames were accomplished in IDL by matrix multiplication.

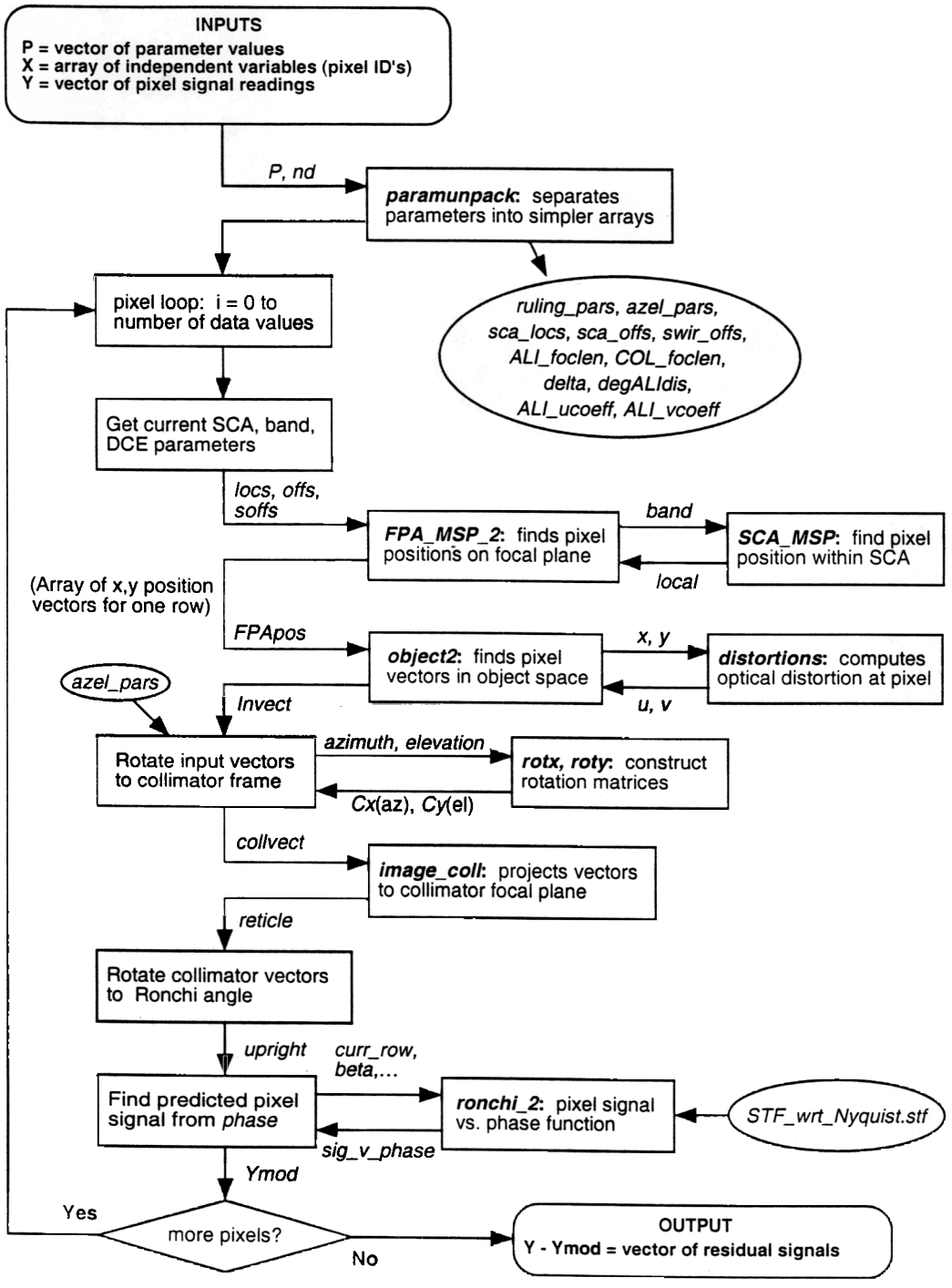

Figure 12. Flow chart of losfunct_2.pro, *the function procedure to compute modeled detector signals and subtract them from the measured detector signals.*

4.2.3 Diagnostic Plots

It proved essential to plot the modeled detector signals over the measured ones, in order to verify whether or not the fitting process was converging to a valid set of parameters. This we did for each static image, one band at a time. All four SCA's were plotted, but the odd and even-numbered detectors were plotted separately, making eight plots per band. This was done because the odd-even stagger of the detectors causes very confusing plots for the 60° and 120° Ronchi orientations. Samples of these diagnostic plots are shown in Figure 13 and Figure 14.

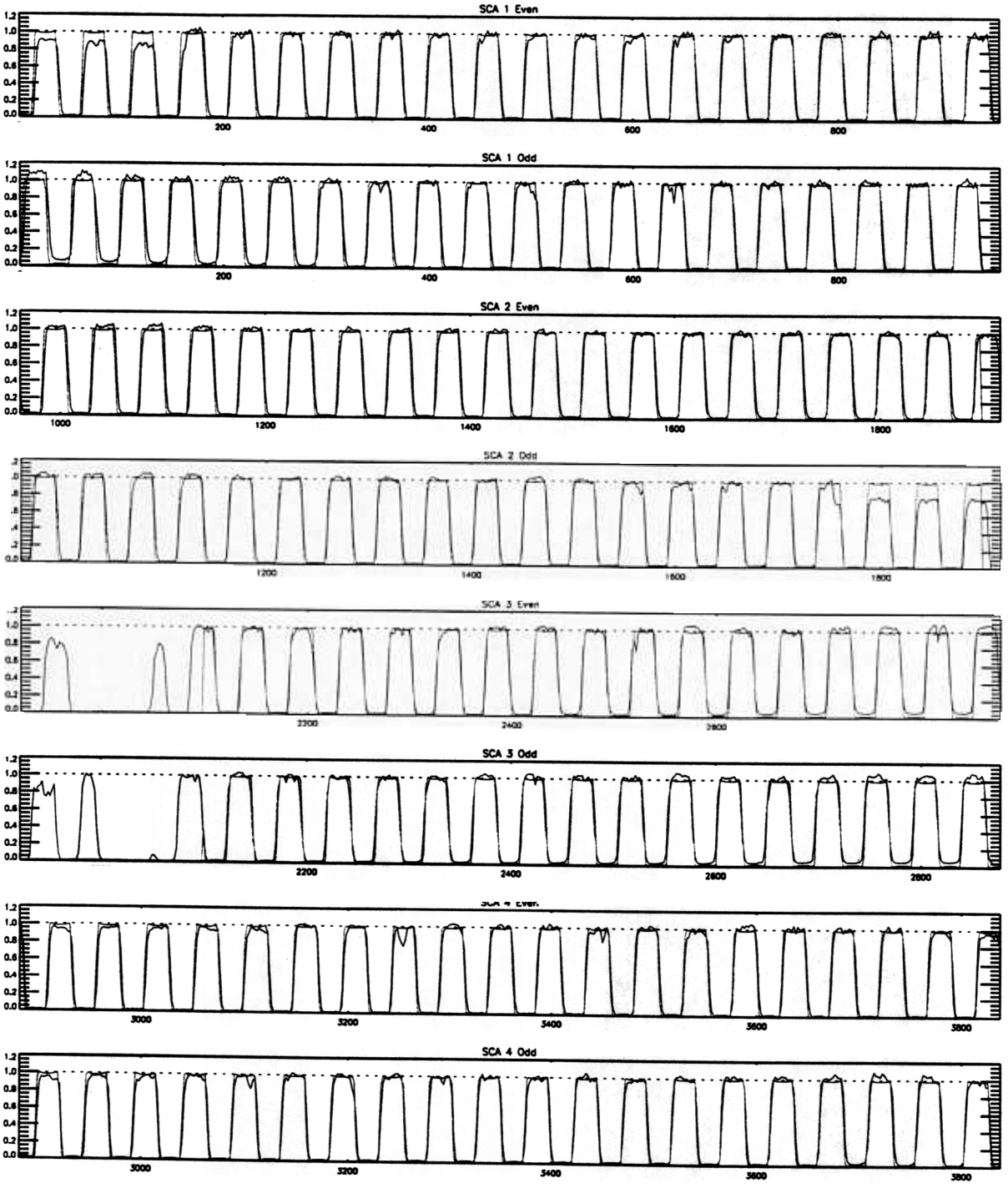

Figure 13. Measured detector signals and modeled signals (in red) for the Pan Band, 59.47° Ronchi orientation.

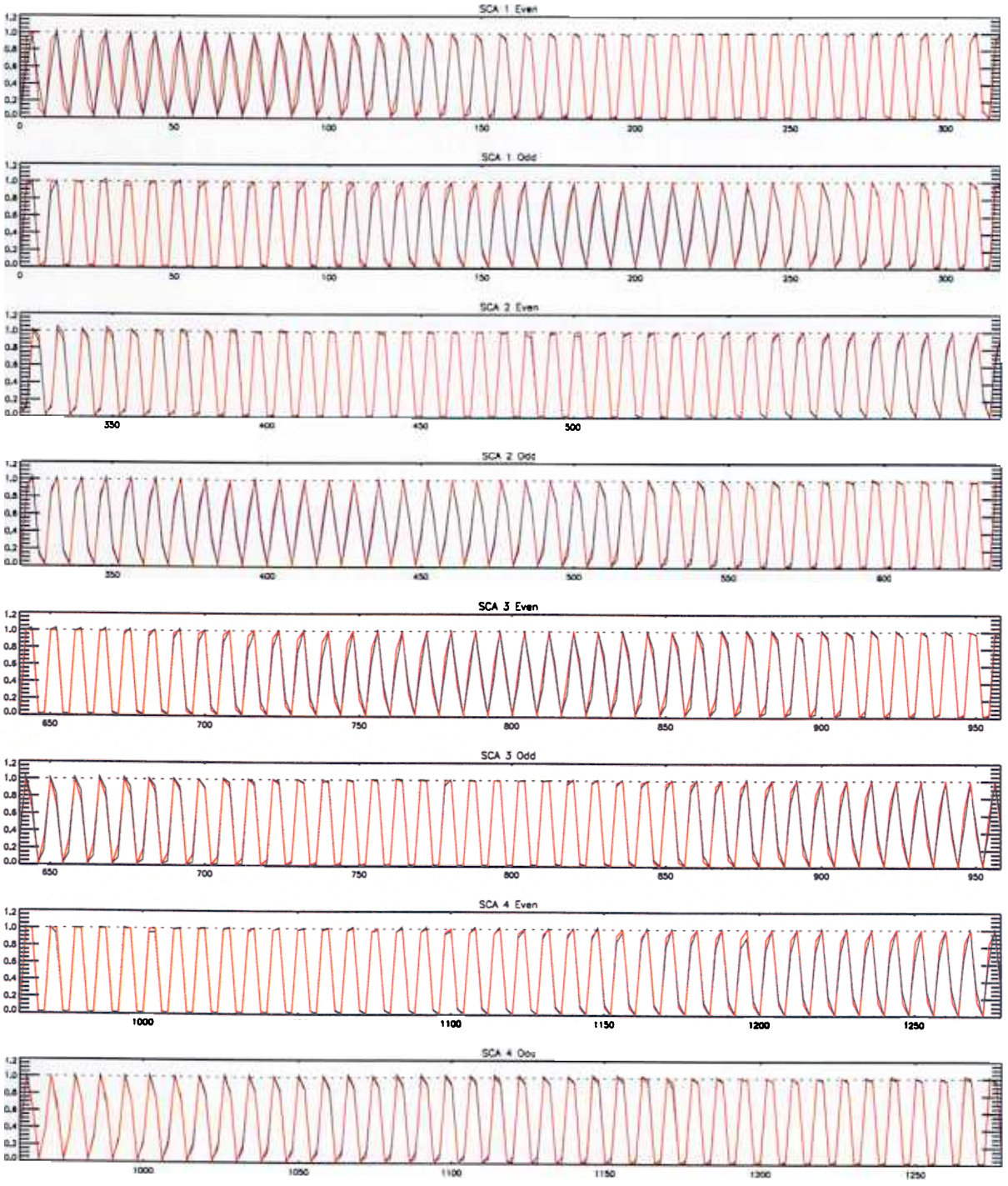

Figure 14. Measured detector signals and modeled signals (in red) for Band 7, 0.33° Ronchi orientation.

Telescope Focal Length and Distortions

By the nature of the laboratory testing setup, the focal length of the ALI telescope can not be determined from the image fits independently of the collimator focal length. The fits can only tell us that the ratio of the ALI focal length to the collimator focal length is 0.63445. If we use the design value of the collimator focal length, which is 1485.94 mm, then the ALI focal length is 942.761 ± 0.003 mm. Theodolite measurements of the ALI telescope indicated a focal length of 942.436 ± 0.005 mm. The discrepancy between these two values probably arises from an error of 0.5 mm in the collimator focal length. Analysis of images from on-orbit operations may permit a refinement of the ALI focal length determination.

Distortion polynomial coefficients for the linear terms in X and Y are highly correlated with the telescope focal length. We have generally fixed those terms at zero. The telescope however, could be anamorphic. In the final analysis, the in-track (X) distortion term linear in X position was left free.

Results of Parameter Fitting

To visualize the meaning of the parameters resulting from the fit to the Ronchi images, plots have been constructed to show the vector difference between actual LOS positions on the focal plane and corresponding ideal LOS positions in the absence of distortions or alignment errors. The scales of the vectors are much larger than the position scales, and are generally indicated by drawing a multispectral detector at the scale of the vectors.

There is excellent agreement between the subsystem measurement and the Ronchi fit. Figure 15 shows the optical distortion field. The top panel shows the distortion estimated from SSG subsystem measurements. The middle panel shows the distortion fitted to Ronchi ruling images. The bottom panel plots the difference of the two fits, also showing the locations of the SCA's. In each case, the small square drawn at the center of the field indicates the size of a multispectral detector (39.6x40.0 μm) at the scale of the distortion vectors. The fit is poorest at the end of the field opposite to the detector array, where there is no data to constrain the Ronchi fit. Fortunately, that has no influence on the lines-of-sight computed for the detectors.

Figure 16 is a plot showing only the region of the focal plane near the MS/Pan array. It shows locations of the detector rows and offsets of the SCA's from their nominal locations, as vectors. The origins of the SCA vectors are at the positions of fiducial marks used during assembly of the array. The SWIR sub-array offset vectors are placed at the ends of the Band 7 rows. The black arrows are from the subsystem measurement, and the red arrows resulted from the end-to-end fit. Again, a square 40 μm detector "pixel" is plotted at the scale of the vectors. Some of the difference between the subsystem and end-to-end estimates could be caused by the filters, which were not part of the LOS model.

Figure 17 is a plot similar to Figure 16. It shows locations of the detector rows, the offsets of the SCA's, and the optical distortion field, all at the same scale, indicated by the 40 μm square detector "pixel."

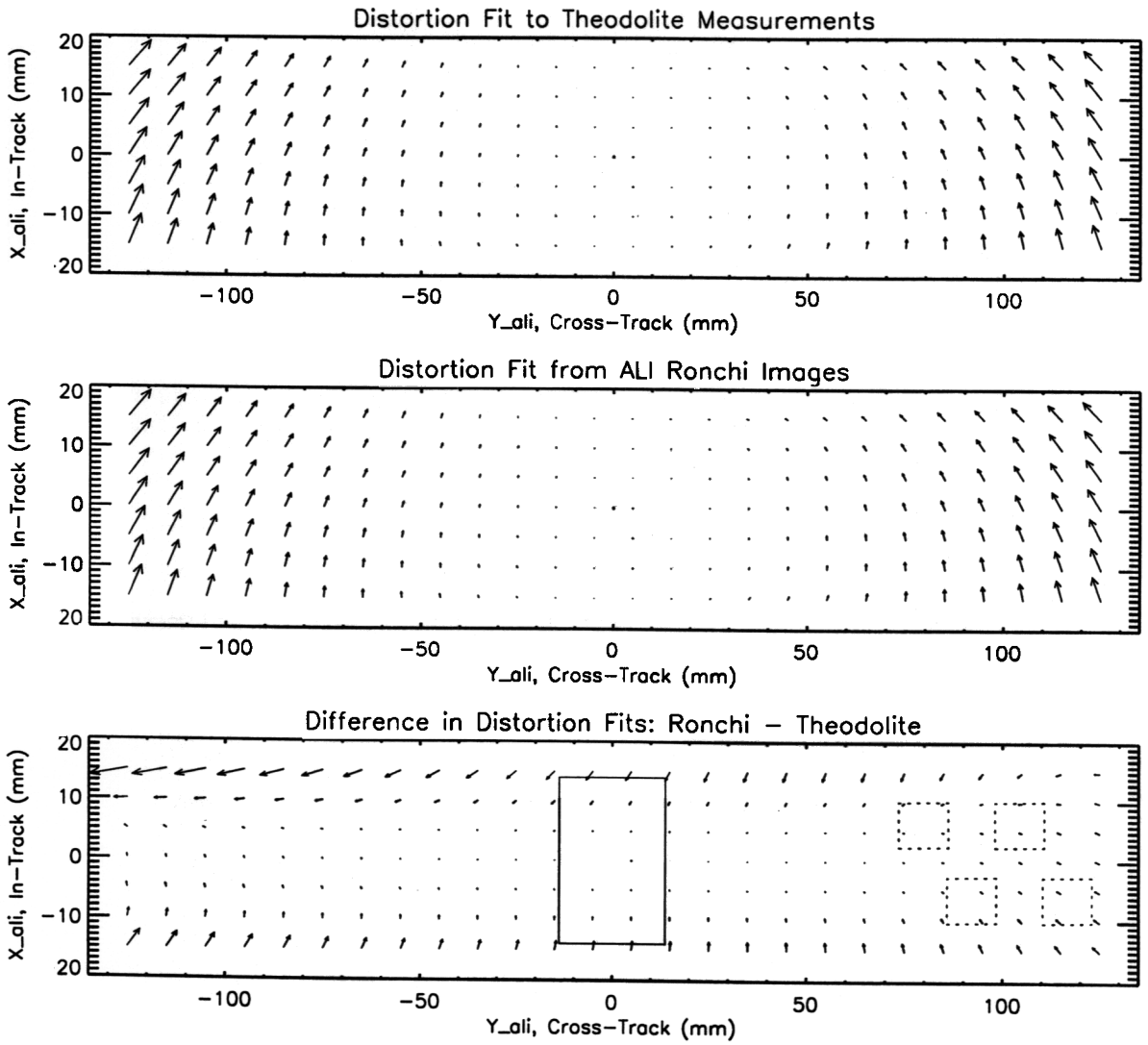

Figure 15. Comparison plots of optical distortion over the entire ALI field of view.

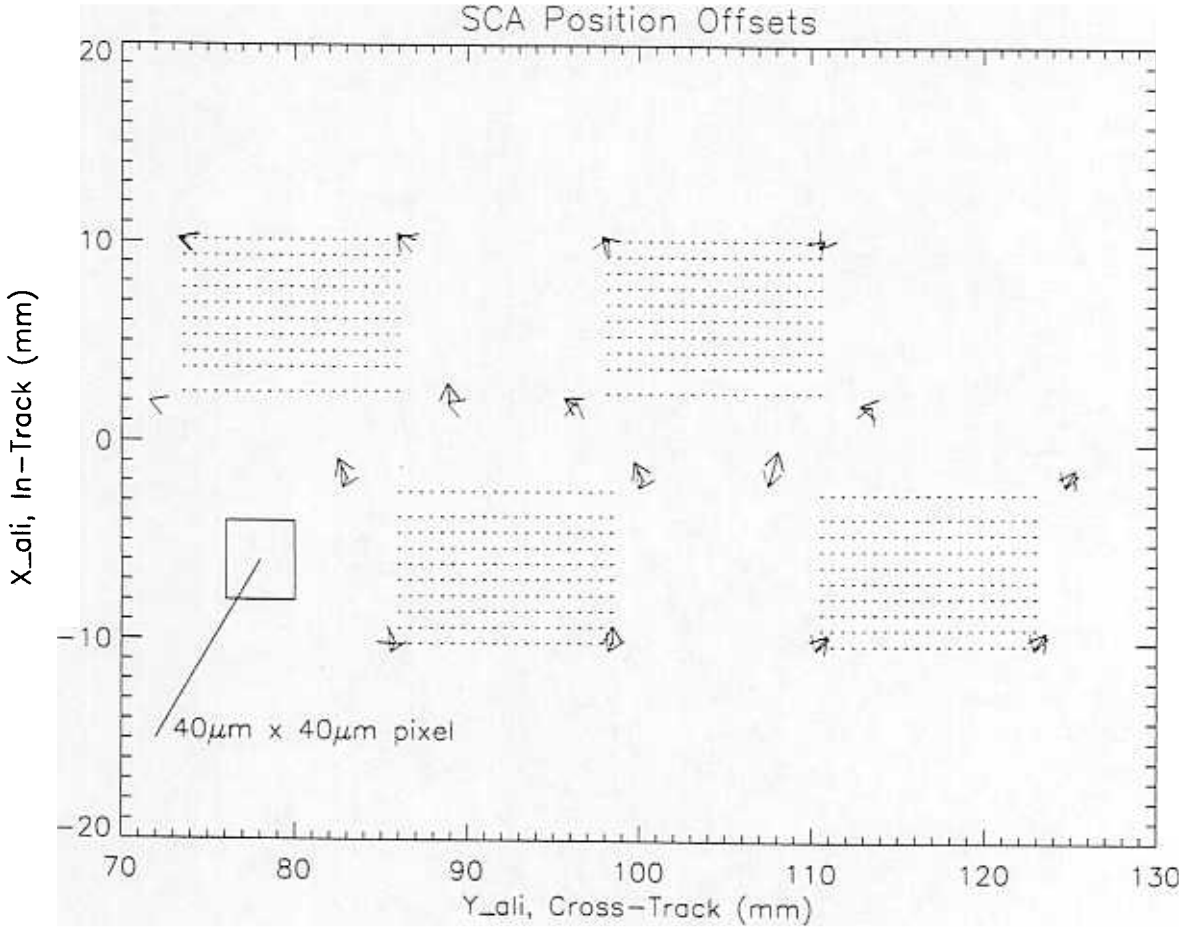

Figure 16. Displacements of the sensor chips from their designed locations.

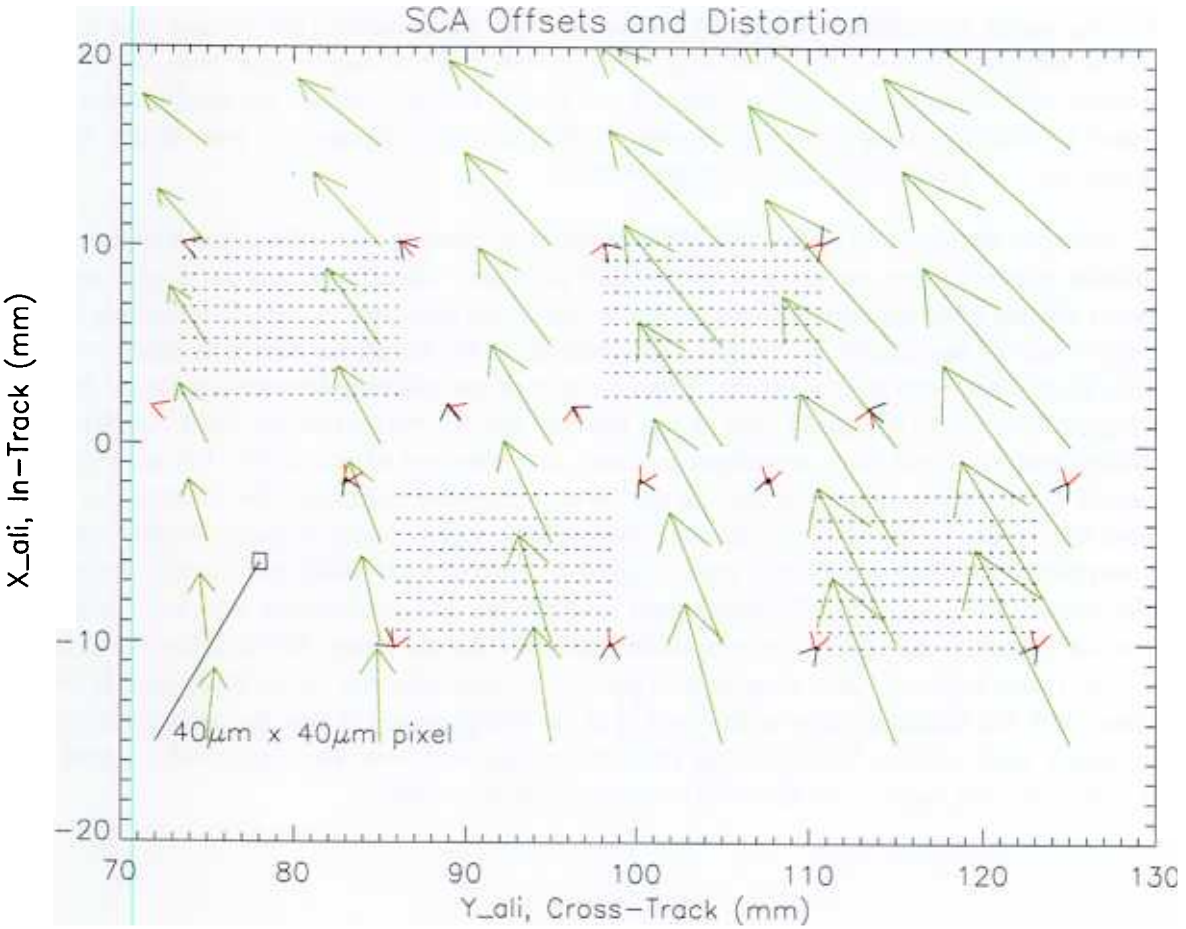

Figure 17. Vector plot of the MS/Pan end of the focal plane.

4.2.6 Lessons Learned

While the development of the software procedures to model and fit the detector signals was a major task, some seemingly trivial items caused far more trouble than the mathematical algorithms. We tried to maintain consistency in referring all coordinates to a Cartesian frame with its axes parallel to the nominal spacecraft axes, namely X along the velocity vector, Z towards nadir (the telescope axis), and Y to make a right-handed system. The X, Y origin was the nominal center of the ALI focal plane. Unfortunately, when the theodolite measurements were performed at SSG, the ALI X axis pointed toward the floor. SSG, following established tradition, reported the measurements in a system with X horizontal, and Y up. Distortion-fitting procedures we developed at Lincoln Laboratory simply used the same definitions for

convenience. Later, when the end-to-end LOS calibration was to be analyzed, this proved to be a continuing source of confusion. To clarify the terminology, we designated the various axes X_{ALI}, or Y_{SSG}, etc. Thus we have $Y_{SSG} = -X_{ALI}$, and $X_{SSG} = Y_{ALI}$. In retrospect, it would have been better to start by converting all SSG data to the ALI reference frame before further analysis. Yet another reference frame was used by SBRS in designing the focal plane array. Those axes, X_M and Y_M, were simply rotated 180° from X_{ALI} and Y_{ALI}, and did not cause too much trouble.

When we attempted to derive the LOS parameters by running *mpfit*, the process appeared to run to completion without errors, but some of the resulting parameter values were very far from those expected. Since we did not have accurate estimates of the errors on the measured signals, the resulting chi-squared value (χ^2) was not necessarily indicative of the goodness of fit. Numerous runs were made with different starting parameters, with similar results. When we plotted the modeled detector signals (as in Figure 13 and Figure 14) over the measured ones, it was apparent that the "fits" were not valid. The Ronchi cycles (measured and modeled) were sometimes in phase, and often out of phase. The fits were finding local minimum χ^2 values in parameter space, but not the correct, global minimum. We realized that many such minima must exist, owing to the oscillatory nature of the signals being modeled. Finally, careful study and iteration of the diagnostic signal plots allowed us to find better initial estimates of key parameters. These included the ratio of the collimator focal length to the ALI focal length, which we estimated from the vertical-Ronchi image. Next, the orientation angles and Ronchi phases for the other two images (~60° and ~120°) were adjusted. Once these critical parameters were adjusted, the modeled signals were nearly in phase with the measured ones at the start, and the fitting process found the global minimum χ^2. In retrospect, a much coarser Ronchi ruling could have been used here, and a successful global fit would have been much less sensitive to the initial estimates of the parameters.

5 DETECTOR LINE-OF-SIGHT MAP

The end product of our line-of-sight calibrations is a data file to be used for the reconstruction of ALI images. An IDL procedure has been developed to read the output data from the end-to-end parameter fitting procedure, and apply those parameters to reconstruct the LOS of every detector. The resulting detector LOS map file is then read by an image reconstruction procedure, and stored in a table.

5.1 LINE-OF-SIGHT MAP FILE CONTENTS

We have chosen to represent the detector lines-of-sight as *apparent* positions of the detectors on the ALI focal plane, in units of millimeters. These are used in conjunction with a specified ALI focal length to find the angular lines of sight. Instead of computing angles, however, we generally find it simpler to work with vectors. For example, given a detector position (x_d, y_d) on the focal plane, the corresponding (un-normalized) line-of-sight vector is $(-x_d, -y_d, f_{ALI})$.

The map file is in ASCII text format. It includes at the beginning the ALI focal length. This is preceded by three lines of header text, and followed by two more header lines. The following lines (15,360 of them) give the positions of all detectors. On each line are the band code, SCA number, pixel number within the SCA (0 to 319 or 0 to 959), and finally the X (in-track) and Y (cross-track) positions in mm. The current and best LOS map file is named "LOS_Oct_31_00.dat.LOS."

5.2 SIMPLE IMAGE RECONSTRUCTION

A full Earth-referenced image reconstruction from on-orbit data collection requires all of the spacecraft position and attitude data mentioned earlier. A simpler image reconstruction can be done however, whether from on-orbit data or data collected in the laboratory. For this we need the detector LOS map file, and good estimates of the scan speed and scan yaw angle. Two procedures were developed in IDL to do this simple reconstruction for scanned images recorded in the laboratory. For these scans, the target at the focal plane of the imaging collimator was translated vertically (in the X direction) at a speed simulating the apparent orbital scan motion. The simplest procedure, called *ALI_remap.pro*, simply shifts the data samples in time (i.e., frame number) to align the various bands and SCA's in the in-track direction. A more exact procedure, called *ALI_resample5.pro*, interpolates (re-samples) the data, using the LOS map information. Inputs to both of the IDL procedures included the scan speed (in mm/sec at the ALI focal plane). The re-sampling procedure also uses an input yaw angle. This was necessary because the alignment of the scan slide did not exactly match the ALI X-axis.

The procedure *ALI_resample5.pro* writes a file containing all of the re-sampled image data, including redundant readings from overlapping detectors at the ends of the SCA's. Another IDL procedure, *Viewit4.pro*, reads that file and displays as much of it as will fit in the user's plotting window.

The central detector and frame number (column and row pixel) are input variables. Currently for the MS images, Bands 1, 2, and 3 are displayed as blue, green and red components. Since there is a ten MS-detector overlap between the adjacent SCA's, this procedure currently displays the abutted images by dropping the last five pixels from one SCA and the first five from the next SCA. The procedure also writes a file of the displayed RGB image in JPEG format.

5.3 TEST IMAGES

A check on the validity of the LOS map and the image reconstruction procedures was done on a scan of a photographic transparency. The transparency was sandwiched between two sheets of glass at the image plane of the collimator. A small portion of the image is seen in Figure 18. The boundary between SCA 2 and SCA 3 detector data passes through the triangular window area just to the left of center in the figure.

Figure 18. Reconstructed ALI image recorded from a photographic transparency scan.

At the time the Ronchi ruling static images were recorded, scanned images were also made. These were displayed in the clean room by the quick-look software, as a check on the equipment setup. One of these images has also been reconstructed with the final line-of-sight map. The central portion of the Pan image of the nominal 60° Ronchi target is shown in Figure 19. The diameter of the outer bulls-eye ring at the ruling is 6 millimeters. The boundary between SCA 2 and SCA 3 passes near the center of the

innermost circle. The overlaid bulls-eye was on a transparency from a laser printer, and there appear to be numerous stray particles of toner near the bulls-eye.

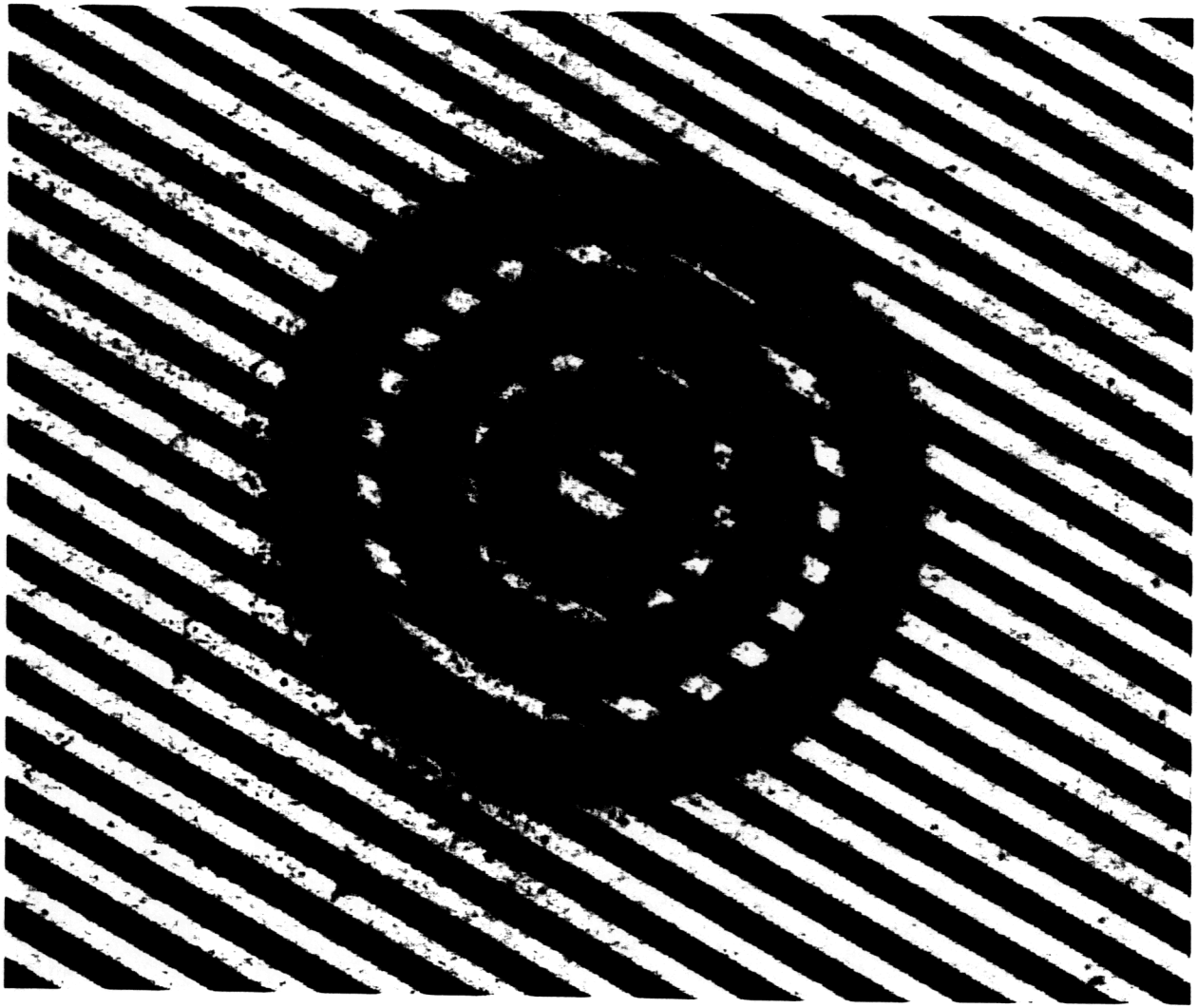

Figure 19. Pan band image of the Ronchi ruling at 60°.

6 SPECTRAL PURITY

For a multispectral Earth-imaging system such as this, it is important to sample the scene at the very same locations in all bands. This is the requirement of "spectral purity." To sample the same location with this type of instrument, the corresponding detectors of the different bands have to be aligned to follow exactly the same ground track. The ALI sensor is unable to meet this requirement simultaneously for all detectors in its array, because of the optical distortion. Examination of Figure 17 reveals that the detectors in different bands appear to be at different cross-track positions. Furthermore, optical distortion also changes the apparent band-to-band spacing, making it impossible to choose a single frame rate to provide co-located spectral samples across the whole array.

With the detector line-of-sight map constructed, we can evaluate the degree to which the apparent displacement of the corresponding detectors in different bands limits the spectral purity attainable with the ALI.

6.1 LINEAR APPROXIMATION OF THE OPTICAL DISTORTION

The optical distortion field around the MS/Pan detector array, seen most clearly in Figure 17, has considerable regularity. Over any limited area on the focal plane, this distortion can be linearly approximated as a translation, a rotation, and a re-scaling. Figure 20 shows the residual distortion remaining around the MS/Pan detector array, after subtraction of a vector offset (ΔY, ΔX) of (-214., 279.) μm, a yaw rotation of –6.49 mrad, and applying anamorphic magnification factors of (0.9935, 0.9984). The scale of the vectors is indicated by size of the rectangle representing one MS detector. The maximum residual distortion is then 73.3 μm, occurring in the (123, 10.2) mm corner above SCA 1.

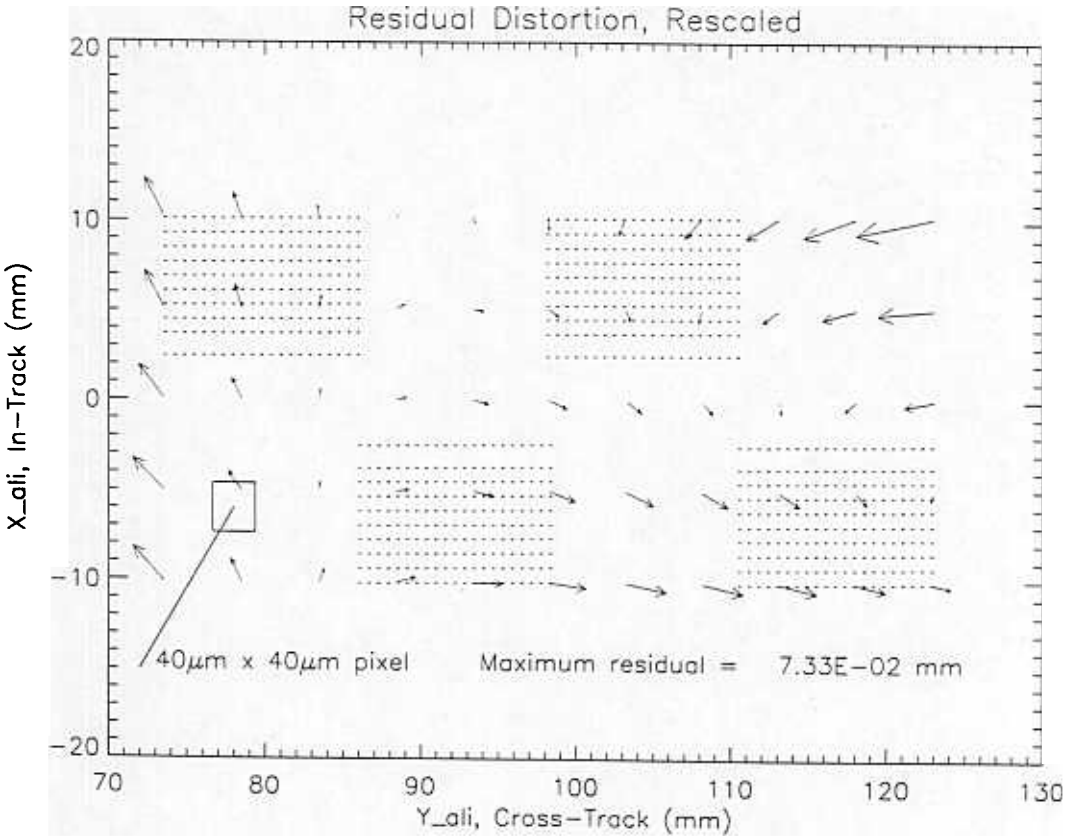

Figure 20. Residual optical distortion around the MS/Pan detector array, after application of a linear coordinate transformation.

6.2 OPERATIONAL IMPLICATIONS FOR THE ALI

As we have just seen, a linear transformation in the focal plane coordinates can greatly reduce the effects of optical distortion. From Figure 20, we observe that if the spacecraft yaw angle and focal plane frame rate are correctly chosen, the difference in sampling positions on the ground for the bands of any chosen SCA can be minimized.

In Figure 21, we plot the mismatch in the sampling locations between Band 1′ and Band 7, for an image collection in which the yaw and frame rate are chosen to minimize the average mismatch across the whole MS/Pan array. The solid curve is the cross-track component, and the dotted curve is in-track. The mismatches are expressed in units of pixels, or GSD. Figure 22 is the same type of plot, but assuming

that only SCA 4 (the most inboard SCA) is optimized. Bands 1′ and 7 are the most widely separated, so they represent the worst case for sampling mismatch.

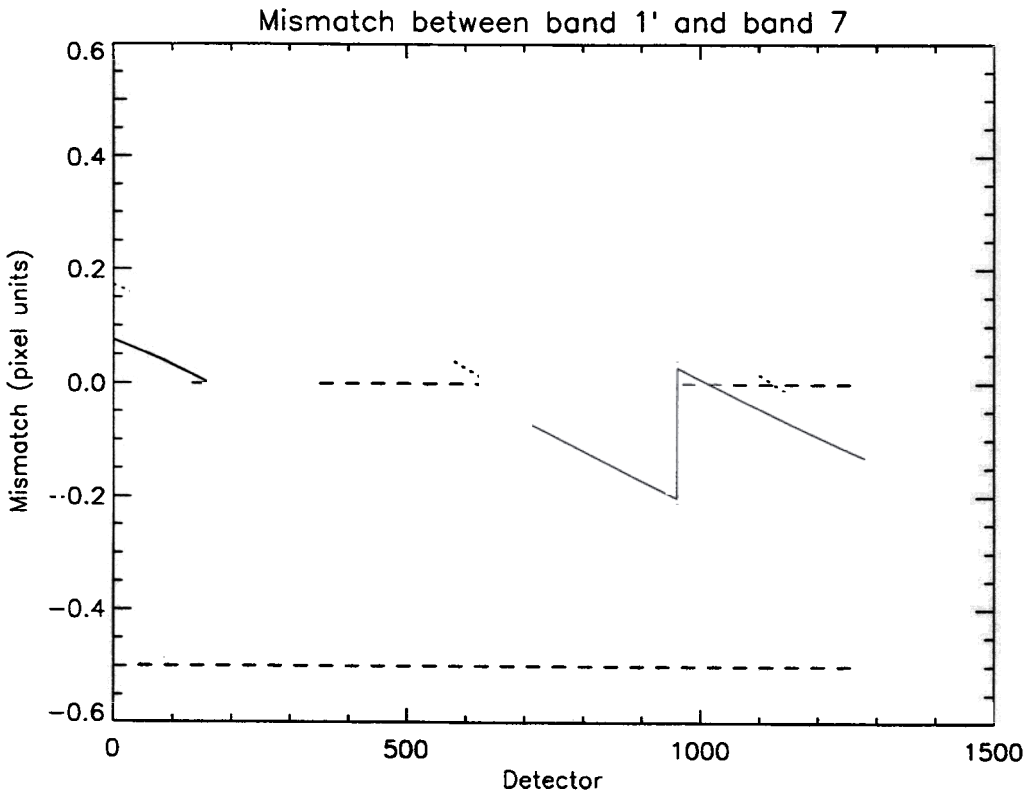

Figure 21. Sampling mismatches from Band 1′ to Band 7, optimized for entire MS array.

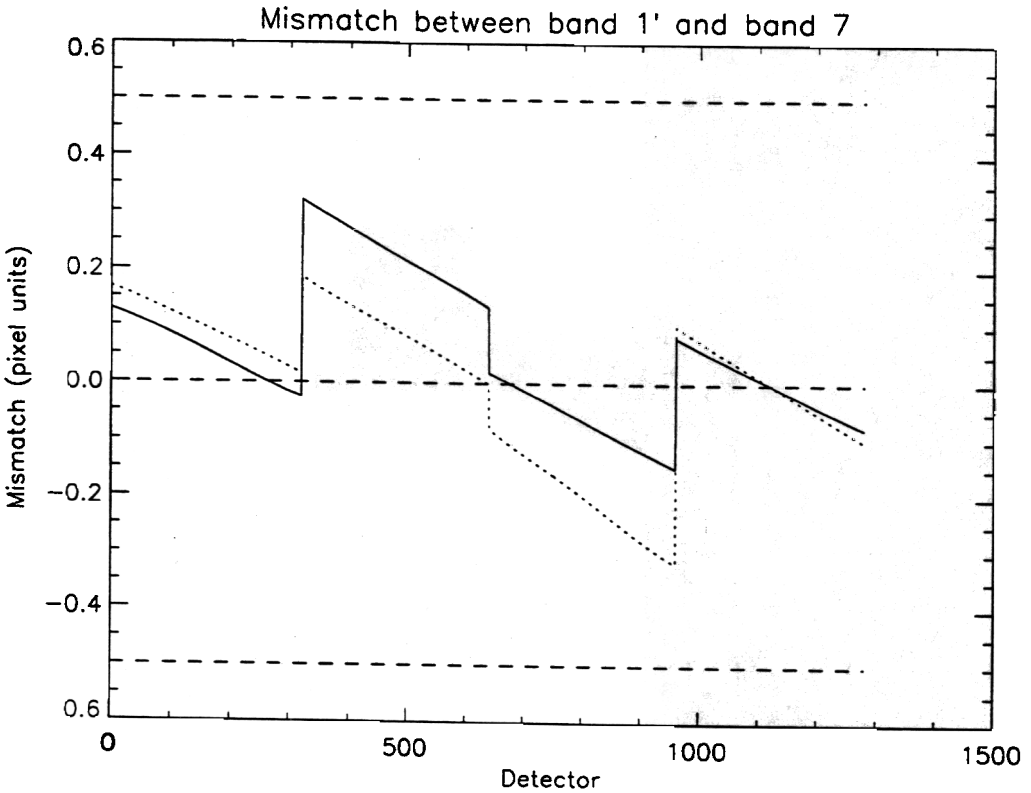

Figure 22. Sampling mismatches from Band 1′ to Band 7, optimized for SCA 4.

Another way to describe spectral purity is to compute the overlap area between image samples in different bands. The geometry is sketched in Figure 23. Bands A and B are sampled with a spatial offset (Δx, Δy) in units of the pixel size. Neither Δx nor Δy can be greater than 1/2, otherwise the next pixel would be used. We may define the spectral purity of the two samples as the fractional overlap area between the two pixels, which is $(1 - \Delta x)(1 - \Delta y)$. Plots of the ALI spectral purity between Bands 1′ and 7 are shown in Figure 24 and Figure 25 for the two cases evaluated for Figure 21 and Figure 22. It should be remembered that the spectral purity calculations shown here represent the best values attainable with the ALI as it presently exists. Any errors in frame rate, yaw angle or attitude control will tend to degrade the overall purity performance.

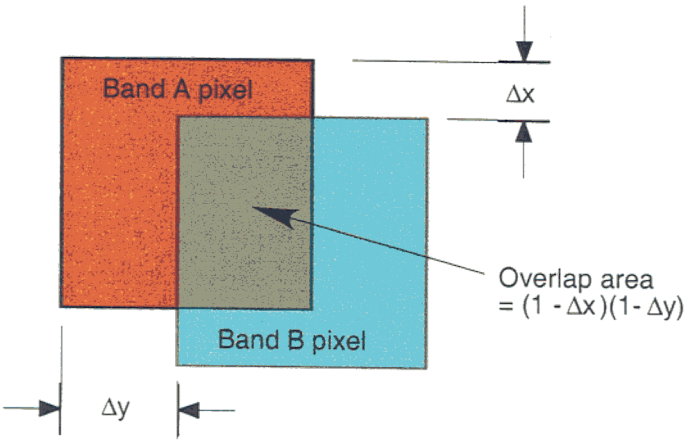

Figure 23. Spectral purity defined as overlap area (sketch).

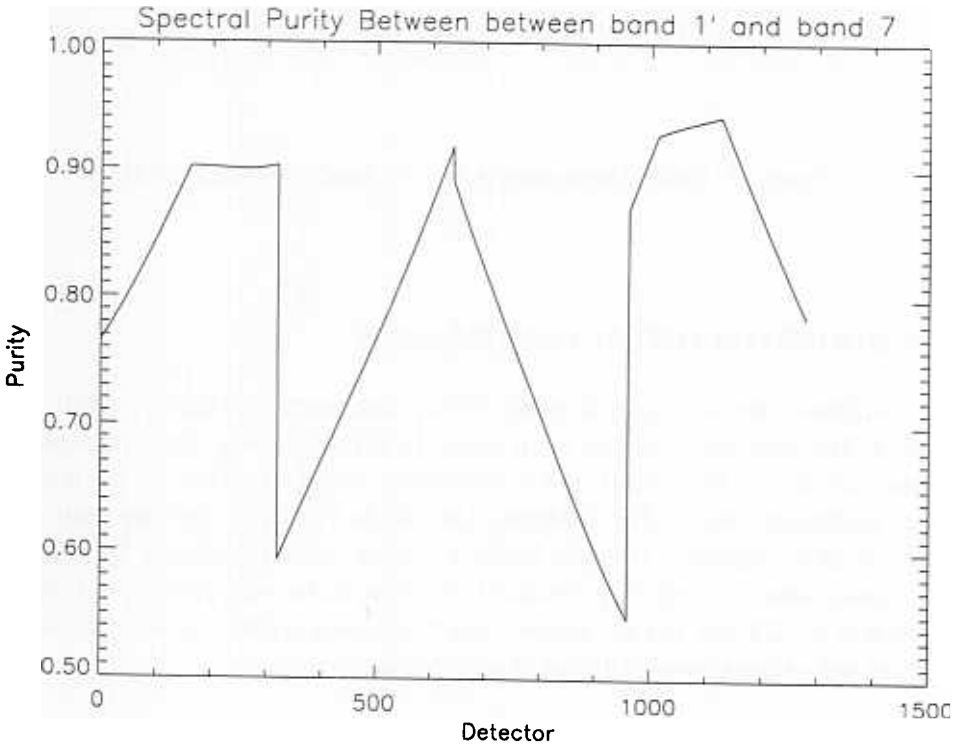

Figure 24. Spectral purity from Band 1' to Band 7, optimized for entire MS array.

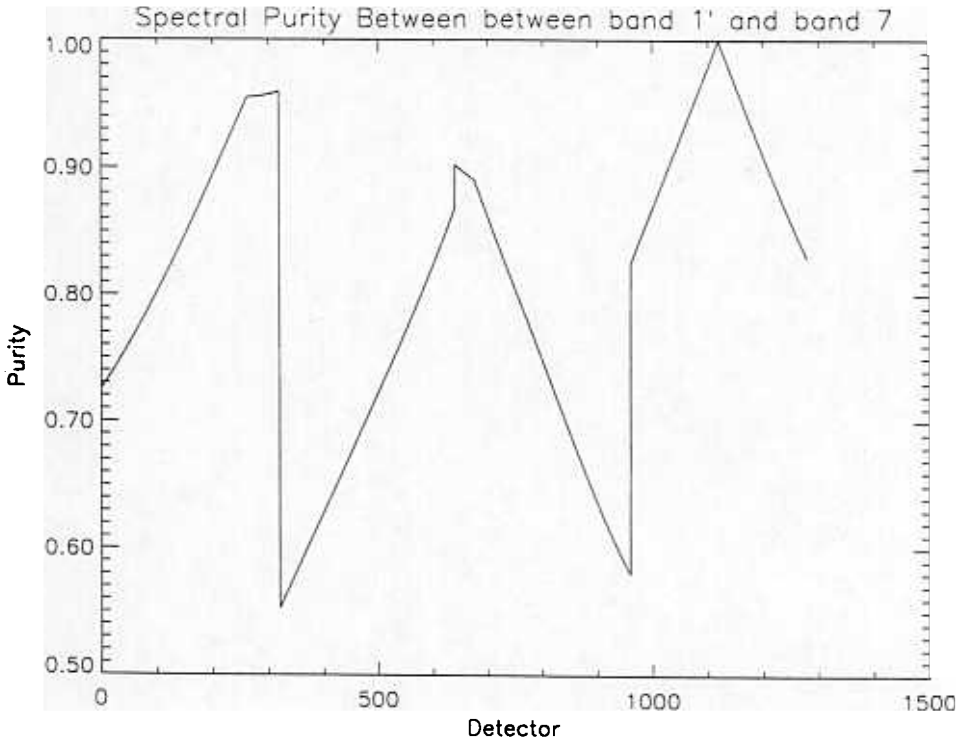

Figure 25. Spectral purity from Band 1′ to Band 7, optimized for SCA 4.

6.3 IMPLICATIONS FOR FUTURE LAND IMAGERS

In order to obtain the best spectral purity, future instruments of this type will have to overcome optical distortion. The best course would be to make the distortion very small through improved optical design. In case that is not successful, the sensor chips could be offset in position and rotation to approximate an undistorted result. For example, referring to Figure 21, the segments of the solid curve representing cross-track mismatch between bands would be shifted vertically by small rotations of the SCA's. In any case, control of the SCA locations will have to be very precise, ~ 1 μm. The worst-case mismatch at present is 12.8 μm. On the sensor chips themselves, a closer spacing of the multiple spectral bands will further reduce the effects of distortion and rotational errors.

7 REFERENCE CUBE ALIGNMENT

The end-to-end measurements described in the preceding sections provided the detector lines of sight relative to the ALI telescope axes. This section describes the measurements made on the ALI instrument to determine the angular relationships of the focal plane lines of sight relative to the external reference cube. That cube is mounted on the ALI pallet, and is intended to provide an angular reference during satellite integration for alignment with the inertial reference unit and the other optical instruments.

All measurements took place with the ALI in a fixed position in the clean room. It was placed on the Flotron fixture under the Class 100 hood, with the *X*-axis pointing down and the *Z*-axis horizontal. The reference cube was approximately 43 inches above the floor, and the center of the entrance pupil approximately 51 inches from the floor.

David Hearn of MIT Lincoln Laboratory and Marcello Benech of SSG made these measurements. To confirm the correct alignment, both individuals viewed all sightings. No readjustments of the theodolite focus were made during the whole series.

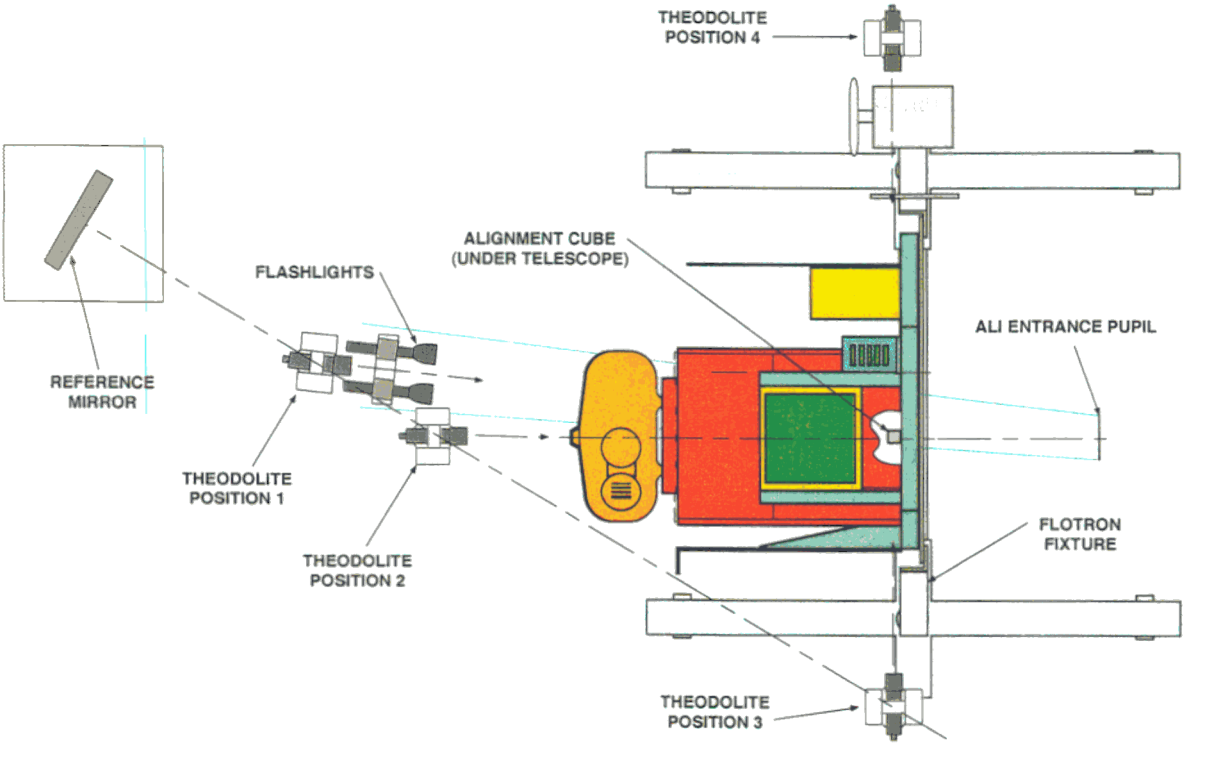

Figure 26. Plan view of clean room setup to measure alignment of the ALI reference cube.

7.1 BASIC SETUP

Equipment used for these measurements included an electronic autocollimating theodolite (Zeiss model Eth 2), a sturdy tripod for the theodolite, a 12-inch flat mirror in a gimbaled mount, and a stable portable platform for the mirror. A pair of Maglite flashlights were also mounted to a bar supported on a tripod in front of the theodolite in order to illuminate the focal plane. A plan view of the equipment positions is shown in Figure 26.

There were four distinct positions of the theodolite. Positions 1, 2, and 3 were along a line normal to the center of the reference flat mirror, which was kept in a fixed position. The detectors were sighted from position 1. The front of the reference cube was sighted from position 2, and the right side of the cube from position 3. The left side of the cube was sighted from position 4.

7.2 PROCEDURE

7.2.1 Detector Sighting

The theodolite was first placed in position 1, which was chosen to provide the least obstructed view of the Sensor Chip Assemblies on the focal plane. The flashlights were placed to each side of and just in front of the theodolite. They were adjusted to give the clearest view of the detectors when looking through the theodolite. It was found to be possible to see the Panchromatic Band arrays of all four SCA's.

After the theodolite was leveled, and put through its setup procedure, measurement readings were made of the azimuth and elevation angles of the Pan detector arrays. Figure 27 shows the appearance of the focal plane when looking into the ALI. A sketch of the "sight pictures" for the detector measurements is presented in Figure 28. Each end of each SCA Pan array was measured. The crosshairs were set at the end of the double row of Pan detectors, and midway between top and bottom of the two rows.

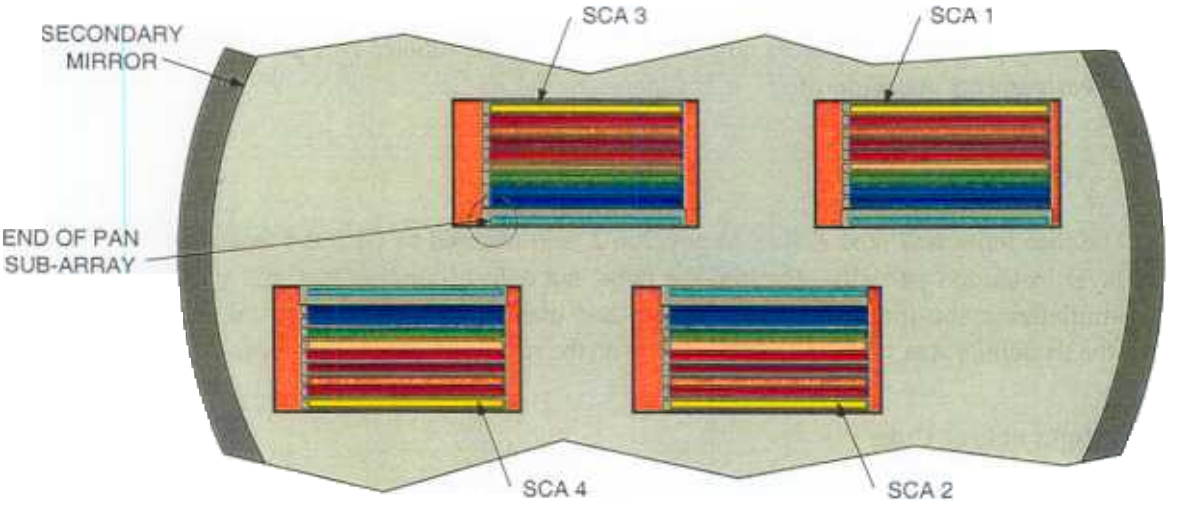

Figure 27. View of the ALI focal plane, as seen through the telescope.

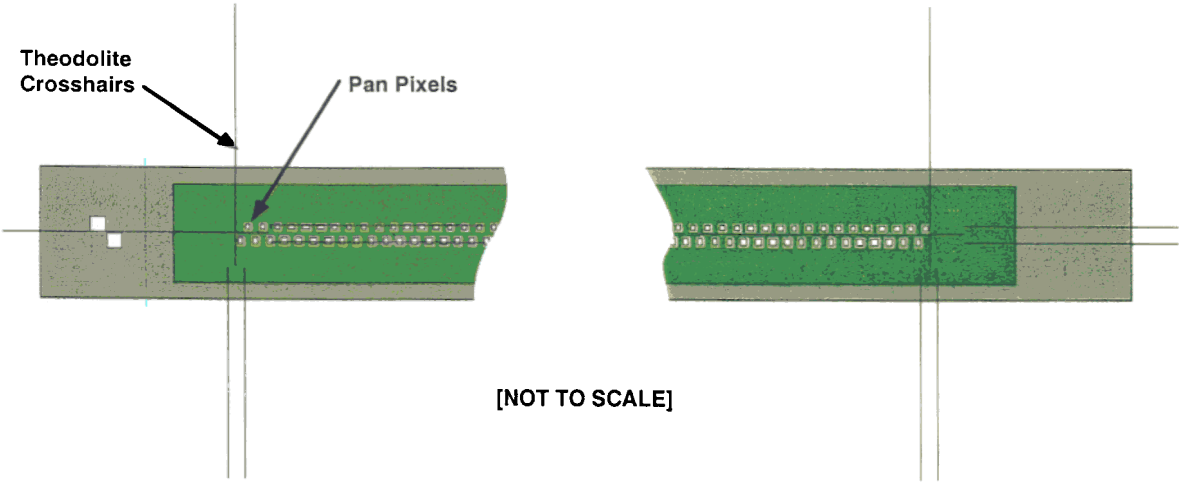

Figure 28. Sight pictures through the theodolite when the crosshairs are correctly aligned with either end of the Pan detector sub-array.

Next, the theodolite was turned to view the fixed reference mirror. Readings were taken when the autocollimating projected lines were aligned with the sighting reticle. This provides an azimuth reference for the measurements in position 1.

Front Face of Cube

The theodolite was next moved to position 2, and lowered to view the front (+*Z*) face of the cube. Multi-layer insulation partially obscured the cube, but autocollimation was still possible. After leveling and re-initializing the theodolite, the azimuth and elevation readings were taken in autocollimation. Again, the theodolite was turned to autocollimate on the reference mirror, and those angles were recorded.

Right Side of Cube

The same procedure was followed for the right (+*Y*) side face as for the front, after moving the theodolite to position 3.

Left Side of Cube

Finally, the theodolite was moved to position 4. Azimuth and elevation readings were taken in autocollimation on the left (-*Y*) side face of the cube. Since this position was not in line with the normal to the reference mirror, the reference readings were not possible. That information however, would be redundant, since the angle between that cube face and the front face had been measured previously. One side face of the cube is sufficient to provide the angular references, but both were measured so that either of the faces could be used during subsequent alignments.

7.3 ANGULAR MEASUREMENTS

All elevation measurements are referred to the local vertical, which is automatically determined by the theodolite to an accuracy of 0.5 arc seconds. The azimuth reference for each position of the theodolite is arbitrary, but the accuracy is the same as for the elevation axis. Experience of the operators has shown that sightings of the same target are repeatable to approximately ± 1 arc second.

Panchromatic Detectors

TABLE 4 lists the readings taken at the ends of each of the Pan arrays. The column labeled "Azimuth" gives the direct theodolite readings. The "Relative Azimuth" column gives the angles relative to the front face of the reference cube. All angles are in decimal degrees.

TABLE 4

Angular Readings of the Pan Detector Arrays (in Degrees)

SCA	Side	Elevation	Azimuth	Relative Azimuth
1	Right	-0.1156	2.9944	7.6478
1	Left	-0.1157	2.2208	6.8741
2	Right	-0.4184	2.2543	6.9077
2	Left	-0.4184	1.4840	6.1373
3	Right	-0.1167	1.5085	6.1618
3	Left	-0.1170	0.7383	5.3916
4	Right	-0.4189	0.7696	5.4229
4	Left	-0.4189	359.9952	4.6486
Reference Flat		-0.6008	215.0613	—

7.3.2 Cube Faces

TABLE 5 gives the theodolite readings in autocollimation from the visible faces of the cube. As previously mentioned, reference flat readings were not taken in position 4. The relative azimuth for that face had previously been measured to be 90° 0′ 7″.

TABLE 5

Angular Readings of the Reference Cube Faces (in Degrees)

	Elevation	Azimuth	Relative Azimuth
Theodolite Position 2			
Front face of cube (+Z)	0.0756	3.9260	0.0000
repeat:	0.0756	3.9261	
Reference Flat	-0.5996	223.6407	
Theodolite Position 3			
Side face of cube (+Y)	0.0286	331.5060	-90.0001
Reference Flat	-0.6008	281.2207	
Theodolite Position 4			
Side face of cube (-Y)	-0.0256	21.6465	90.0019

7.4 ROTATION TO CUBE-BASED COORDINATES

For the purpose of alignment, the frame of reference for the detector lines of sight is defined as follows: The Z-axis is the normal to the $+Z$ face of the reference cube. The Y-axis is in the plane determined by this normal and the normal to the $+Y$ face of the cube (which is orthogonal to the $+Z$ normal to within 1 arc-second). The X-axis is orthogonal to the other two, forming a right-handed coordinate system.

Since the ALI was not situated with its X-axis exactly vertical during the present measurements, the angular readings must be transformed to the cube frame of reference. This has been accomplished with vector algebra and rotation matrices.

7.4.1 Vectors in the Laboratory Frame

Angular readings are first converted into vectors in the laboratory frame, bearing in mind that the X-axis pointed down, the Z-axis was at zero relative azimuth, and the Y-axis was at $-90°$ azimuth:

$$
\begin{aligned}
x &= \sin(\varepsilon) \\
y &= -\sin(\alpha)\cos(\varepsilon) \quad , \\
z &= \cos(\alpha)\cos(\varepsilon)
\end{aligned}
\tag{1}
$$

where α = the relative azimuth, and ε = the elevation angle.

The resulting vectors are listed in TABLE 6. Ends of the Pan sub-arrays are listed as "1 Right," "3 Left," etc.

TABLE 6

Sighting Vectors in the Laboratory Frame

Vectors	Laboratory Axis		
	X	Y	Z
Pan Points			
1 Right	-0.002018	-0.133082	0.991103
1 Left	-0.002019	-0.119689	0.992809
2 Right	-0.007302	-0.120266	0.992715
2 Left	-0.007302	-0.106909	0.994242
3 Right	-0.002037	-0.107337	0.994221
3 Left	-0.002042	-0.093963	0.995574
4 Right	-0.007311	-0.094505	0.995498
4 Left	-0.007311	-0.081041	0.996684
Cube Faces			
+Z	0.001319	0.000000	0.999999
+Y	0.000499	1.000000	-0.000001
-Y	-0.000447	-1.000000	-0.000034

Rotation Matrices

The vectors were first rotated about the Laboratory Y-axis by $\theta = -0.0756°$ to bring the normal of the front cube face to coincide with the Z-axis. Then they were rotated about the Z-axis by $\phi = 0.0286°$ to bring the normal to the +Y cube face horizontal. In matrix algebra, this is expressed as:

$$\begin{pmatrix} x_c \\ y_c \\ z_c \end{pmatrix} = \begin{pmatrix} \cos\phi & -\sin\phi & 0 \\ \sin\phi & \cos\phi & 0 \\ 0 & 0 & 1 \end{pmatrix} \begin{pmatrix} \cos\theta & 0 & \sin\theta \\ 0 & 1 & 0 \\ -\sin\theta & 0 & \cos\theta \end{pmatrix} \begin{pmatrix} x_l \\ y_l \\ z_l \end{pmatrix} \tag{2}$$

where subscripts l and c denote the laboratory and cube frames, respectively.

The product of the two individual matrices gives the resultant rotation matrix, which is, in numerical form,

0.999999	-0.000499	-0.001319
0.000499	1.000000	-0.000001
0.001319	0.000000	0.999999

Vectors and Angles in the Cube Frame

Application of the rotation matrix to the sighting vectors listed in TABLE 6 results in the cube-referenced vectors as listed in TABLE 7. For convenience, the corresponding azimuth and elevation angles are listed as well.

TABLE 7

Direction Vectors in the Cube Frame

Vectors	Reference Axis			Angles (degrees)	
	X	Y	Z	Azimuth	Elevation
Pan Points					
1 Right	-0.003259	-0.133084	0.991099	7.6479	-0.1867
1 Left	-0.003270	-0.119690	0.992806	6.8743	-0.1873
2 Right	-0.008552	-0.120270	0.992704	6.9080	-0.4900
2 Left	-0.008561	-0.106914	0.994231	6.1377	-0.4905
3 Right	-0.003295	-0.107339	0.994217	6.1620	-0.1888
3 Left	-0.003309	-0.093965	0.995570	5.3918	-0.1896
4 Right	-0.008577	-0.094509	0.995487	5.4233	-0.4915
4 Left	-0.008586	-0.081046	0.996673	4.6488	-0.4919
Cube Faces					
+Z	0.000000	0.000000	1.000000	0.0000	0.0000
+Y	0.000000	1.000000	0.000000	-90.0000	0.0000
-Y	0.000052	-1.000000	-0.000035	90.0020	0.0030

7.5 TELESCOPE OPTICAL AXES IN THE CUBE REFERENCE FRAME

The positions sighted on the focal plane through the theodolite are all within the MS/Pan detector array, and do not correspond with the axes of the ALI telescope. In contrast, the *relative* lines of sight derived from the end-to-end Ronchi images are based on the telescope axes. We now need to relate the telescope axes to the ALI reference cube axes.

We see in TABLE 7 a set of eight vectors called "Pan points." These correspond with relative lines of sight of detectors at the ends of the Pan array of each SCA. From the LOS map file, we take the Y (cross-track) position of each end detector, and the average X (in-track) position of the odd and even end detectors to be the nominal sighted location. Using the fitted telescope focal length, the eight unit LOS vectors in the telescope frame were constructed. They are listed in TABLE 8.

TABLE 8

Direction Vectors in the Telescope Frame

Vectors	Optical Axis		
	X	Y	Z
Pan Points			
1 Right	0.003131	-0.129842	0.991530
1 Left	0.003046	-0.116589	0.993176
2 Right	-0.002232	-0.117034	0.993125
2 Left	-0.002322	-0.103737	0.994602
3 Right	0.002957	-0.104093	0.994563
3 Left	0.002883	-0.090775	0.995867
4 Right	-0.002385	-0.091222	0.995828
4 Left	-0.002463	-0.077870	0.996960

Vectors in the telescope frame should be related to vectors in the cube frame by a three-dimensional rotation of coordinates. To within measurement uncertainties, all eight vector pairs should be related by the same transformation. Symbolically, this may be stated as:

$$\mathsf{R} \cdot \mathsf{A} = \mathsf{T} \ , \tag{3}$$

where

A = the matrix of column-vectors in the telescope frame (eight in this case),

T = the matrix of column-vectors in the reference-cube frame, and

R = the 3x3 rotation matrix which transforms vectors from the telescope frame to the cube frame.

The transpose of A is listed in TABLE 8, and TABLE 7 contains the transpose of T. We desire a solution of Equation (3) for R, in the least-squares sense, in order to relate the telescope axis vectors to the reference cube frame. We proceed as follows:

Equation (3) is first transposed to find

$$\mathsf{A}^{\mathsf{T}} \cdot \mathsf{R}^{\mathsf{T}} = \mathsf{T}^{\mathsf{T}} \tag{4}$$

The least-squares solution of (4), according to Strang [9], is:

$$\mathsf{R}^{\mathsf{T}} = \left(\mathsf{A} \cdot \mathsf{A}^{\mathsf{T}}\right)^{-1} \cdot \mathsf{A} \cdot \mathsf{T}^{\mathsf{T}} \tag{5}$$

Applying Equation (5) to the A and T matrices and transposing the result, we find

$$\mathsf{R} = \begin{pmatrix} 0.99915 & 0.00558 & -0.00570 \\ 0.00544 & 1.00072 & -0.00315 \\ 0.00689 & 0.00334 & 0.99999 \end{pmatrix} \tag{6}$$

The R matrix is an approximation to the matrix for the small rotation from the telescope frame to the reference-cube frame. For *small* rotation angles, the rotation matrix is the identity matrix plus a differential matrix, [10]

$$\mathsf{R}' \approx \mathsf{1} + \varepsilon \quad , \tag{7}$$

$$\varepsilon = \begin{pmatrix} 0 & d\Omega_3 & -d\Omega_2 \\ -d\Omega_3 & 0 & d\Omega_1 \\ d\Omega_2 & -d\Omega_1 & 0 \end{pmatrix} \tag{8}$$

where $d\Omega_1$, $d\Omega_2$, and $d\Omega_3$ are the differential rotation angles about the X, Y, and Z axes, respectively. To the degree that equation (7) is a valid approximation, the three rotations about the axes may be performed in any order, with the same result. Let us call the three rotation angles α, β and γ. Comparing equations (6) and (8), we arrive at the following estimates for the three angles:

$$\alpha = -0.186 \pm 0.005 \text{ degees}$$

$$\beta = 0.361 \pm 0.034 \text{ degees}$$

$$\gamma = 0.004 \pm 0.316 \text{ degees}$$

The uncertainty in γ is much greater than for the other two angles, because that angle represents the rotation about the telescope axis, and the two ends of the MS/Pan array which was measured with the theodolite are separated by only 3°. Uncertainty in that angle also leads to greater uncertainty in the β angle about the Y (elevation) axis.

Finally, we construct a rotation matrix to transform vectors from the telescope frame to the reference cube frame. First, a matrix B rotates by α about the X axis, then C rotates by β about the Y axis, then D rotates by γ about the Z axis. (Each rotation moves the coordinate axes in a right-handed sense.)

$$\mathsf{B} = \begin{pmatrix} 1 & 0 & 0 \\ 0 & \cos\alpha & \sin\alpha \\ 0 & -\sin\alpha & \cos\alpha \end{pmatrix}, \quad \mathsf{C} = \begin{pmatrix} \cos\beta & 0 & \\ 0 & 1 & \\ \sin\beta & 0 & \end{pmatrix}, \quad \mathsf{D} = \begin{pmatrix} \cos\gamma & \sin\gamma & 0 \\ -\sin\gamma & \cos\gamma & 0 \\ 0 & 0 & 1 \end{pmatrix}, \text{ and}$$

$$\mathsf{DCB} = \begin{matrix} \cos\beta\cos\gamma + \sin\alpha\sin\beta\sin\gamma & \cos\alpha\sin\gamma & -\sin\beta\cos\gamma + \sin\alpha\cos\beta\sin\gamma \\ -\cos\beta\sin\gamma + \sin\alpha\sin\beta\cos\gamma & \cos\alpha\cos\gamma & \sin\beta\sin\gamma + \sin\alpha\cos\beta\cos\gamma \\ \cos\alpha\sin\beta & -\sin\alpha & \cos\alpha\cos\beta \end{matrix}$$

Inserting the three angles in Equation (10), we find the overall rotation matrix:

$$\boxed{\mathsf{DCB} = \begin{pmatrix} 0.99998 & 0.00007 & -0.00630 \\ -0.00009 & 0.99999 & -0.00324 \\ 0.00630 & 0.00324 & 0.99997 \end{pmatrix}. \qquad (11)}$$

The three column vectors of the DCB rotation matrix represent the X, Y, and Z axes of the ALI telescope in the frame of the reference cube. This rotation matrix must be applied the detector LOS vectors to express them also in the reference cube frame.

APPENDIX A
ALI LINE-OF-SIGHT PARAMETERS

In all, 82 formal parameters were employed in the analysis of the Ronchi ruling images to derive the relative detector lines-of-sight. They fall into several categories. First, there is a group of parameters to describe the laboratory conditions, listed in TABLE A-1. They are essential in performing the least-squares fit, but do not enter into the detector LOS construction. A second group characterizes the positions of the sensor chip assemblies on the focal plane assembly. The final group describes the properties of the ALI optical system.

TABLE A-1

Ronchi Ruling and Collimator Parameters

Index No.	Description	Fitted Value	Formal Error
File number 16799:			
0	Ronchi beta angle (degrees)	-1.76774	0.00033
1	Ronchi frequency (cycles/mm)	2.00000	fixed
2	Ronchi -collimator phase	0.85856	0.00010
File number 16807:			
3	Ronchi beta angle (degrees)	59.38534	0.00014
4	Ronchi frequency (cycles/mm)	2.00000	fixed
5	Ronchi -collimator phase	0.27717	0.00011
File number 16809:			
6	Ronchi beta angle (degrees)	119.60982	0.00017
7	Ronchi frequency (cycles/mm)	2.00000	fixed
8	Ronchi -collimator phase	0.10186	0.00013
Collimator Parameters:			
9	azimuth (degrees)	-5.940	fixed
10	elevation (degrees)	-0.214	fixed
48	collimator focal length (mm)	1485.940	fixed

The position of a sensor chip assembly is described by the X and Y coordinates, relative to the center of the focal plane, of a reference fiducial in the metallization layer, and a rotation angle. The position parameters were separated into design value parameters, which were left fixed, and offset parameters, which had nominal values near zero. The design value parameters are listed in TABLE A-2, and the offset parameters are listed in TABLE A-3. In addition, the SWIR detectors were formed in a separate chip, bump-bonded onto the sensor chip. To allow for placement errors of the SWIR detector chip, a similar set of offset parameters, shown in TABLE A-4, was provided for the SWIR detectors of each SCA. The software procedure which calculates the position of each detector within the sensor chip has an implicit set of parameters derived from the chip layout design.

TABLE A-2

Sensor Chip Assembly Position Design Parameters

Index No.	Description	Value	Formal Error
SCA 1, Design Values:			
11	X, in-track (mm)	-1.887	fixed
12	Y, cross-track (mm)	124.780	fixed
13	Rotation angle (degrees)	180.000	fixed
SCA 2, Design Values:			
14	X, in-track (mm)	1.887	fixed
15	Y, cross-track (mm)	96.309	fixed
16	Rotation angle (degrees)	0.000	fixed
SCA 3, Design Values:			
17	X, in-track (mm)	-1.887	fixed
18	Y, cross-track (mm)	100.226	fixed
19	Rotation angle (degrees)	180.000	fixed
SCA 4, Design Values:			
20	X, in-track (mm)	1.887	fixed
21	Y, cross-track (mm)	71.755	fixed
22	Rotation angle (degrees)	0.000	fixed

TABLE A-3

Sensor Chip Assembly Position Offset Parameters

Index No.	Description	Fitted Value	Formal Error
SCA 1:			
23	X, in-track (mm)	0.00693	0.00011
24	Y, cross-track (mm)	0.00499	0.00006
25	Rotation angle (degrees)	-0.02946	0.00060
SCA 2:			
26	X, in-track (mm)	0.00349	0.00007
27	Y, cross-track (mm)	-0.00699	0.00006
28	Rotation angle (degrees)	-0.00833	0.00040
SCA 3:			
29	X, in-track (mm)	0.00971	0.00012
30	Y, cross-track (mm)	-0.00544	0.00005
31	Rotation angle (degrees)	-0.00247	0.00065
SCA 4:			
32	X, in-track (mm)	0.00047	0.00000
33	Y, cross-track (mm)	-0.00147	0.00000
34	Rotation angle (degrees)	0.03398	0.00036

TABLE A-4

SWIR Detector Chip Position Offset Parameters

Index No.	Description	Fitted Value	Formal Error
SCA 1:			
35	X, in-track (mm)	-0.00184	0.00026
36	Y, cross-track (mm)	0.01337	0.00023
37	Rotation angle (degrees)	0.03366	0.00156
SCA 2:			
38	X, in-track (mm)	-0.00937	0.00025
39	Y, cross-track (mm)	0.00473	0.00027
40	Rotation angle (degrees)	-0.01970	0.00166
SCA 3:			
41	X, in-track (mm)	0.00955	0.00025
42	Y, cross-track (mm)	0.00971	0.00023
43	Rotation angle (degrees)	0.04161	0.00154
SCA 4:			
44	X, in-track (mm)	-0.00810	0.00022
45	Y, cross-track (mm)	0.00485	0.00026
46	Rotation angle (degrees)	-0.02439	0.00151

The line-of-sight parameters related to the ALI optical system are the focal length of the telescope and the coefficients of the distortion polynomials. One more parameter was initially coded into the software to allow a cross-track offset of the optical axis for the distortion polynomials. It is listed here for completeness, but it was fixed at zero throughout our fitting process.

TABLE A-5

ALI Telescope Parameters

Index No.	Description	Fitted Value	Formal Error
47	ALI focal length (mm)	942.7609	0.0027
49	Optical axis offset (mm)	0.00	fixed

The optical distortion polynomials were constructed in the coordinate frame employed in the SSG theodolite measurements. The necessary transformations to ALI coordinates were coded in the fitting software. The equations for the distortion polynomials are:

$$u = \sum_{i=0}^{3}\sum_{j=0}^{3} A_{ij}\left(\frac{X_S}{100}\right)^i\left(\frac{Y_S}{100}\right)^j$$

and

$$v = \sum_{i=0}^{3}\sum_{j=0}^{3} B_{ij}\left(\frac{X_S}{100}\right)^i\left(\frac{Y_S}{100}\right)^j$$

where X_S and Y_S are the SSG focal plane coordinates in millimeters (see Figure 8), and u and v are the distortion components in the X_S and Y_S directions, respectively. (The coordinates were scaled by factors of 100 in order to make the coefficient values less extreme.) The fitted values of the coefficients A_{ij} and B_{ij} are tabulated in TABLE A-6 and TABLE A-7.

TABLE A-6

Coefficients of the u Distortion Polynomials, A_{ij}

	j = 0		1		2		3	
i = 0	50[a]	0.00000 fixed	54	0.00000 fixed	58	-0.5938 ± 0.0038	62	7.467 ± 0.037
1	51	0.00000 fixed	55	0.65650 ± 0.00022	59	1.0337 ± 0.0049	63	7.684 ± 0.046
2	52	-0.00024 ± 0.00005	56	0.01695 ± 0.00033	60	0.0253 ± 0.0036	64	-3.526 ± 0.047
3	53	-0.25210 ± 0.00005	57	0.22272 ± 0.00027	61	-0.4578 ± 0.0020	65	-11.379 ± 0.038

[a] Index number of parameter

TABLE A-7

Coefficients of the v Distortion Polynomials, B_{ij}

	j = 0		1		2		3	
i = 0	66	0.00000 fixed	70	0.00164 ± 0.00031	74	-0.1177 ± 0.0030	78	0.147 ± 0.041
1	67	0.00000 fixed	71	-0.13205 ± 0.00038	75	-0.4385 ± 0.0044	79	-3.009 ± 0.057
2	68	-0.32329 ± 0.00006	72	-0.15098 ± 0.00046	76	0.1547 ± 0.0055	80	-1.539 ± 0.062
3	69	0.00466 ± 0.00006	73	0.15106 ± 0.00039	77	0.4943 ± 0.0045	81	-2.187 ± 0.051

GLOSSARY

ALI	Advanced Land Imager
EO-1	Earth Observing-1
FPA	focal plane array
GSD	Ground sampling distance
JPEG	A lossy image-compression standard from the Joint Photographic Experts Group
LOS	line-of-sight
MS	multispectral
Pan	panchromatic
RGB	Red-green-blue image color model
ROIC	read-out integrated circuit
SBRS	Raytheon Santa Barbara Remote Sensing
SCA	sensor chip assembly
SWIR	short-wave infrared
VNIR	visible and near-infrared

REFERENCES

1. Digenis, C. J., Lencioni, D. E., and Bicknell, W. E., "New Millennium Advanced Land Imager," Proc. SPIE, Vol. 3439, pp. 49-55, July 1998.

2. Mendenhall, J. A., Lencioni, D. E., Hearn, D. R., and Parker, A. C., "EO-1 Advanced Land Imager preflight calibration," Proc. SPIE, Vol. 3439, pp. 390-399, July 1998.

3. Mendenhall, J. A., Lencioni, D. E., Hearn, D. R., and Parker, A. C., "EO-1 Advanced Land Imager in-flight calibration," Proc. SPIE, Vol. 3439, pp. 416-422, July 1998.

4. Lencioni, D. E., Hearn, D. R., Mendenhall, J. A., and Bicknell, W. E., "EO-1 Advanced Land Imager calibration and performance overview," Proc. SPIE, Vol. 3750, pp. 89-96, July 1999.

5. Hearn, D. R., Mendenhall, J. A., and Willard, B. C., "Spatial calibration of the EO-1 Advanced Land Imager," Proc. SPIE, Vol. 3750, pp. 97-108, July 1999.

6. Willard, B. C., "Wide field-of-view Schmidt-sphere imaging collimator," Proc. SPIE Vol. 3750, pp. 286-296.

7. Hearn, D. R., "EO-1 Advanced Land Imager Modulation Transfer Functions," MIT Lincoln Laboratory, Technical Report 1061, 22 March 2000.

8. For details on mpfit.pro, go to http://astrog.physics.wisc.edu/~craigm/idl/idl.html, and follow the link to MPFIT.

9. Strang, Gilbert, *Linear Algebra and its Applications*, 3rd Ed., Harcourt Brace Jovanovich, Orlando 1988. (See Chapter 3.)

10. Goldstein, Herbert, *Classical Mechanics*, Addison-Wesley, Reading, 1950. (See Chapter 4.)